INTERIM REPORT

Innovative Processing, Feature Development and Specialized Data Collection for Underwater Munitions Advanced Classifier Design

SERDP Project MR-1713

JUNE 2016

Eugene Lavely
BAE Systems

Distribution Statement A
This document has been cleared for public release

SERDP
DOD ▪ EPA ▪ DOE

This report was prepared under contract to the Department of Defense Strategic Environmental Research and Development Program (SERDP). The publication of this report does not indicate endorsement by the Department of Defense, nor should the contents be construed as reflecting the official policy or position of the Department of Defense. Reference herein to any specific commercial product, process, or service by trade name, trademark, manufacturer, or otherwise, does not necessarily constitute or imply its endorsement, recommendation, or favoring by the Department of Defense.

REPORT DOCUMENTATION PAGE

Form Approved
OMB No. 0704-0188

The public reporting burden for this collection of information is estimated to average 1 hour per response, including the time for reviewing instructions, searching existing data sources, gathering and maintaining the data needed, and completing and reviewing the collection of information. Send comments regarding this burden estimate or any other aspect of this collection of information, including suggestions for reducing the burden, to Department of Defense, Washington Headquarters Services, Directorate for Information Operations and Reports (0704-0188), 1215 Jefferson Davis Highway, Suite 1204, Arlington, VA 22202-4302. Respondents should be aware that notwithstanding any other provision of law, no person shall be subject to any penalty for failing to comply with a collection of information if it does not display a currently valid OMB control number.
PLEASE DO NOT RETURN YOUR FORM TO THE ABOVE ADDRESS.

1. REPORT DATE *(DD-MM-YYYY)*
06/08/2016

2. REPORT TYPE
Interim Report/White Paper

3. DATES COVERED *(From - To)*
April 2010 - December 2015

4. TITLE AND SUBTITLE
Interim Report and White Paper: T-matrix Formulation of Acoustic Target Characterization and Analysis and Discussion of Current and Future Data Supporting its Validation

5a. CONTRACT NUMBER
W912HQ-10-C-0038

5b. GRANT NUMBER

5c. PROGRAM ELEMENT NUMBER

6. AUTHOR(S)
Eugene Lavely
BAE Systems

5d. PROJECT NUMBER
MR-1713

5e. TASK NUMBER

5f. WORK UNIT NUMBER

7. PERFORMING ORGANIZATION NAME(S) AND ADDRESS(ES)
BAE Systems - 6 New England Executive Park, Burlington, MA 01803

Naval Surface Warfare Center Panama City Division,
110 Vernon Avenue, Panama City, FL 32407

8. PERFORMING ORGANIZATION REPORT NUMBER

9. SPONSORING/MONITORING AGENCY NAME(S) AND ADDRESS(ES)
Strategic Environmental Research and Development Program
4800 Mark Center Drive
Suite 17D03
Alexandria, VA 22350-3605

10. SPONSOR/MONITOR'S ACRONYM(S)
SERDP

11. SPONSOR/MONITOR'S REPORT NUMBER(S)

12. DISTRIBUTION/AVAILABILITY STATEMENT
Approved for public release; distribution is unlimited.

13. SUPPLEMENTARY NOTES

14. ABSTRACT
The U.S. Army Corps of Engineers and the Navy have identified more than 400 underwater sites that are potentially contaminated with munitions, and most are in shallow water posing a threat to human safety and the environment. Our objective is to improve low-frequency sonar detection and classification of buried underwater munitions by developing new features that are highly diagnostic of target shape and composition.

15. SUBJECT TERMS
N/A

16. SECURITY CLASSIFICATION OF:			17. LIMITATION OF ABSTRACT	18. NUMBER OF PAGES	19a. NAME OF RESPONSIBLE PERSON
a. REPORT	b. ABSTRACT	c. THIS PAGE			Eugene Lavely
U	U	U	UU	23	19b. TELEPHONE NUMBER *(Include area code)* 781-262-4294

Standard Form 298 (Rev. 8/98)
Prescribed by ANSI Std. Z39.18

Innovative Processing, Feature Development and Specialized Data Collection for Underwater Munitions Advanced Classifier Design (Project MR-1713)

Interim Report and White Paper: T-matrix formulation of acoustic target characterization and analysis and discussion of current and future data supporting its validation.

Submitted by: BAE Systems
6 New England Executive Park, Burlington, MA 01803
***and* Naval Surface Warfare Center Panama City Division,**
110 Vernon Avenue, Panama City, FL 32407

The T-matrix formally encodes the full scattering response of an acoustic target. From it, one may construct the scattered waveform for any given incident waveform. Through a combination of forward modeling, simulated inversions, and processing of real data, this report details basic validation of the approach for characterizing targets of interest. Data set include some collected during Strategic Environmental Research and Development Program project MM-1507 using Florida Atlantic University's 160-channel towed bottom-scanning sonar platform, as well as some collected in the small-scale test bed acoustic facility at NSWC PCD.

DISTRIBUTION STATEMENT A: Approved for public release.

I. INTRODUCTION

This document serves two purposes. First, it is an interim report describing work to date in support of validating the T-matrix approach to acoustic target characterization. Second, it is the requested white paper discussing the utility of our methods if confined to realistic data, for example a single pass of the bottom-scanning sonar (BOSS) sensor with 15 to 30 cm position error. A full and considered answer to the white paper question requires a deep look at existing data, constraints from simulations, and examination of possible geometries for future BOSS data collects that will better support the utility of our methods. A focused summary of the answer to this question, referring back to all of the prior material, is contained in the concluding Sec. VIII.

The T-matrix description of scattering from buried targets requires knowledge of the sediment properties. In Sec. II we discuss how these properties can be extracted from the angle dependence of the direct return. In App. A we discuss in some detail our attempts to use existing MM 1507 BOSS data to this end. At present, the available platform parameter ground truth is inconclusive (e.g., undocumented channel indexing and gain factors), and we propose near-future measurements that will provide definitive tests.

In Sec. III we summarize the T-matrix representation of target scattering. The T-matrix, in principle, provides a universal description of all target-scattering responses, and we propose that its coefficients could be strongly correlated to key target identifying features, such as resonances that lead to strong changes in some T-matrix parameters and not others. The T-matrix is also most appropriate at lower frequencies, where the target diameter is comparable to wavelength (typically, a few kHz). At high frequency there are very large number of non-negligible T-matrix coefficients, and it becomes more appropriate to use ray-based scattering theory instead. Note that lower frequency enables better sediment penetration, supporting the utility of our approach.

In Sec. IV we specialize the general theory to scattering from targets in a homogeneous medium, and buried in a sediment half-space. We compare simulated scattering responses in the two cases, and how the T-matrix enters the geometry of the scattered field. We also present simulated T-matrix parameter inversion results, demonstrating the key importance of measurement aperture (transmitter–receiver angular diversity) in stabilizing inversions.

In Sec. V we begin our discussion of real data by briefly reviewing the properties of chirp pulse waveforms, and the pulse compression operation required to isolated distinct scattering returns. In Sec. VI we use this theory to analyze BOSS data collected using a 4-in sphere. The standoff is such that the angular aperture is very small, and the data is essentially pure backscatter, which then severely restricts the T-matrix parameter information that can be extracted.

In Sec. VII we describe NSWC laboratory scale tank data in which a very large angular aperture is available. The full scattering amplitude $f(\theta)$ for a spherical target is extracted, which directly encompasses all T-matrix information. This data also explicitly illustrates the importance of transmitter-receiver angular diversity.

Finally, as alluded to above, in Sec. VIII we summarize our findings to date, and discuss near-future BOSS platform data collection that will start to fill in the gaps in validating our approach. We also make some suggestions for relatively simple changes to the BOSS geometry that could greatly enhance the angular aperture and significantly enhance the utility of the T-matrix approach.

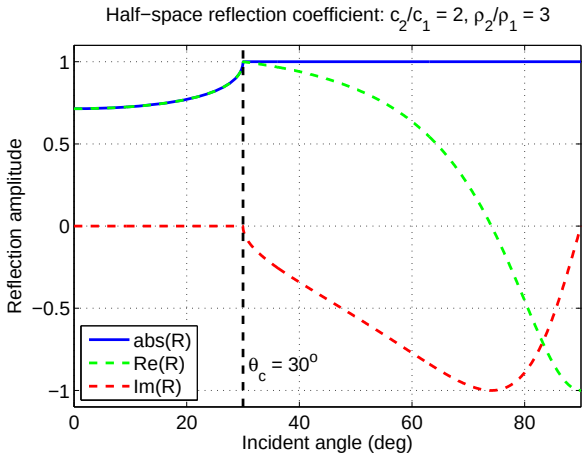

FIG. 1: Reflection coefficient for $\rho_2/\rho_1 = 3$, $c_2/c_1 = 2$. The coefficient becomes complex, but with unit magnitude, beyond the critical (total internal reflection) angle $\theta_c = \sin^{-1}(c_1/c_2)$.

II. MODELING BACKGROUND: SEDIMENT PROPERTIES

Sediment acoustic propagation properties will impact scattering from buried targets. As such, robust interpretation of scattered signals (including standard image focusing) will benefit from proper bottom-sediment modeling. These properties may in principle be extracted through a separate set of direct, bottom-reflection measurements.

A. Water–sediment transmission and reflection coefficients

For a uniform half space the reflection and transmission coefficients, for a plane wave incident on medium 2 from medium 1, are given by [1]

$$\begin{aligned} R &= \frac{\cos(\theta) - (\rho_1/\rho_2)\sqrt{(c_1/c_2)^2 - \sin^2(\theta)}}{\cos(\theta) + (\rho_1/\rho_2)\sqrt{(c_1/c_2)^2 - \sin^2(\theta)}} \\ T &= 1 + R \\ &= \frac{2\cos(\theta)}{\cos(\theta) + (\rho_1/\rho_2)\sqrt{(c_1/c_2)^2 - \sin^2(\theta)}}, \end{aligned} \tag{2.1}$$

in which θ is the angle of incidence (measured from the normal), c_i are the sound speeds, and ρ_i are the mass densities. The transmitted ray angle θ_T is determined, as usual, by Snell's law,

$$\frac{\sin(\theta_T)}{\sin(\theta)} = \frac{c_2}{c_1} \tag{2.2}$$

The critical angle, defined by $\sin(\theta_c) = c_1/c_2$, represents the total internal reflection angle when the sediment sound speed exceeds that of water, as is typical.

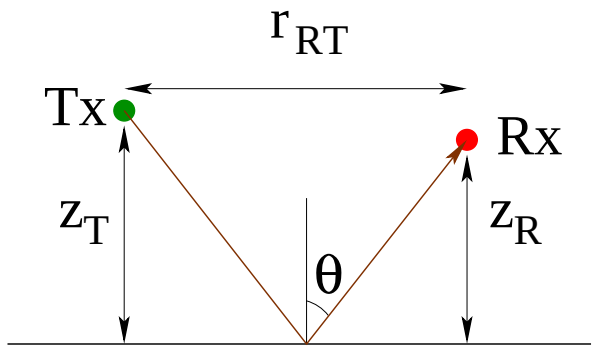

FIG. 2: Bottom reflection geometry for effective point transmitter (Tx) at height z_T, receiver at height z_R, and horizontal separation r_{RT}. The angle of incidence θ is given by (2.4).

For $\theta > \theta_c$ one makes the replacement

$$\begin{aligned} \cos(\theta_T) &= \sqrt{1 - (c_2/c_1)^2 \sin^2(\theta)} \\ &\to i\sqrt{(c_2/c_1)^2 \sin^2(\theta) - 1}, \end{aligned} \tag{2.3}$$

so that T and R become complex. Consistent with total reflection, $R = e^{i\phi_R}$ has fixed unit magnitude, $|R| = 1$, for all $\theta \geq \theta_c$, with ϕ_R generating a phase shift in the reflected signal. The transmitted wave becomes evanescent, reducing the visibility of buried targets. Figure 1 shows a plot of R for physically motivated parameter values.

To invert for the sediment properties (with water properties c_1, ρ_1 assumed known) it would clearly be beneficial to have incident angles spanning θ_c [2]. The singular behavior of R in its vicinity should make it readily identifiable, providing a direct estimate of c_1/c_2. The parameter ρ_1/ρ_2 could then be estimated via an optimized fit of (2.1) to the data over the full range of angles.

In a real measurement, the incident wave is approximately spherical rather than planar, and this must be accounted for in extracting R. Consider, then, idealized point receiver and transmitter at height z_R and z_T, respectively, separated by horizontal distance r_{RT} (see Fig. 2). For wavelengths short compared to the measurement dimensions, a geometrical optics/ray tracing approach is valid, and the reflected ray angle is given by

$$\tan(\theta) = \frac{r_{RT}}{z_R + z_T}, \tag{2.4}$$

and one obtains the total direct-plus-reflected signal

$$\hat{\varphi}(\mathbf{x}_R, \omega) = \hat{A}(\omega)\left[\frac{e^{ikl_D}}{4\pi l_D} + R(\theta)\frac{e^{ikl_R}}{4\pi l_R}\right]. \tag{2.5}$$

where $\hat{A}(\omega)$ is the overall outgoing spherical wave amplitude, $k = \omega/c_1$ is the wavenumber in the fluid, and

$$\begin{aligned} l_D &= \sqrt{r_{RT}^2 + (z_R - z_T)^2} \\ l_R &= \sqrt{r_{RT}^2 + (z_R + z_T)^2} \end{aligned} \tag{2.6}$$

Distribution A / Approved for public release

are the direct and reflected ray path lengths, respectively.

Equivalently, in the time domain, one obtains

$$\varphi(\mathbf{x}_R, t) = \mathrm{Re}\left[\frac{1}{4\pi l_D} P(t - l_D/c_1) + \frac{R(\theta)}{4\pi l_R} P(t - l_R/c_1)\right], \tag{2.7}$$

where $P(t)$ is the positive frequency part of the transmitted pulse waveform:

$$P(t) = \int_0^\infty \frac{d\omega}{2\pi} A(\omega) e^{-i\omega t}. \tag{2.8}$$

Assuming that the travel time difference $(l_R - l_D)/c_1$ is much larger than the inverse bandwidth of the pulse, after pulse compression [where $A(\omega)$ is replaced in (2.8) by $\hat{S}^*(\omega)\hat{A}(\omega)$, where $\hat{S}$ is used to remove rapid phase variation of $\hat{A}$] the two contributions (2.7) can be separated (from each other, as well as from any other bounces, e.g., from the fluid surface). From the known geometry, one may then obtain $R(\theta)$ from the ratio R/l_R. From a receiver array one may then extract $R(\theta)$ over some range of θ.

In a more accurate model, the (frequency dependent) transmitter radiation pattern, and receiver sensitivity pattern, must enter (2.3), making $P(t) \to P(t;\theta)$ angle-dependent. Absent a full characterization of these, one can only hope that the additional angular dependence is weak enough that it suffices to considering only amplitude ratios for different θ, obtained by dividing out a single, unknown, overall amplitude. The assumption is most critical for bottom reflections because the direct ray arrives at a substantially different angle from the buried target reflection, and likely interacts much more strongly with the platform structure. One may thereby extract $R(\theta)/R(\theta_0)$, where θ_0 is some reference angle. This, too, should suffice to extract the desired ratios c_1/c_2 and ρ_1/ρ_2. For example, for small θ one obtains $R(\theta) = R_0[1 + R_2\theta^2 + O(\theta^4)]$ where

$$\begin{aligned} R_0 &= \frac{1 - \rho_1 c_1/\rho_2 c_2}{1 + \rho_1 c_1/\rho_2 c_2} \\ R_2 &= \frac{(\rho_1/\rho_2)(c_1/c_2 - c_2/c_1)}{1 - (\rho_1 c_1/\rho_2 c_2)^2}. \end{aligned} \tag{2.9}$$

If the platform is fully calibrated, then both R_0 and R_2 may be extracted from the measurement, and one obtains

$$\begin{aligned} \frac{\rho_1}{\rho_2}\frac{c_1}{c_2} &= \frac{1 - R_0}{1 + R_0} \\ \frac{\rho_1}{\rho_2}\frac{c_2}{c_1} &= \frac{1 - R_0(R_0 + 4R_2)}{(1 + R_0)^2}, \end{aligned} \tag{2.10}$$

and hence

$$\begin{aligned} \frac{c_1}{c_2} &= \sqrt{\frac{1 - R_0^2}{1 - R_0(R_0 + 4R_2)}} \\ \frac{\rho_1}{\rho_2} &= \sqrt{\frac{(1 - R_0)[1 - R_0(R_0 + 4R_2)]}{(1 + R_0)^3}}. \end{aligned} \tag{2.11}$$

if the platform is uncalibrated, then with adequate bandwidth to resolve direct and reflected returns, we can exploit the geometry based acoustic response ratio between in-plane and boresite ensonification to estimate the incident level along r_{RT}. This allows one to extract both R_0 and R_2 from the small θ region, and thereby both desired ratios. Larger θ, preferably including θ_c are then required for a full inversion [5].

B. Measurement constraints and existing results

In a recent publication, Williams demonstrates the ability to remotely sense sediment properties via acoustic forward scattering measurements [4]. Potential complicating factors such as frequency dependent reflection coefficients and spherical vs. plane wave modeling issues are considered from a theoretical and implementation perspective. Williams concludes that *in situ* measurement of sediment properties has been demonstrated. For a dedicated remote sensing experiment based solely on BOSS system data, the sonar may have to be flown closer to the bottom than is typical of its operation. If there are implementation or deployment difficulties with operating in this close-in measurement mode, then the measurement could be performed sporadically—swooping down for a brief time period to measure a wider range of incident angles than otherwise available.

III. MODELING BACKGROUND: SCATTERING AND THE T-MATRIX

A. Acoustic equation and Green function

The acoustic equation of motion for the pressure field $\varphi(\mathbf{x}, t)$ takes the form

$$\frac{1}{\rho c^2}\partial_t^2 \varphi - \nabla \cdot \left(\frac{1}{\rho}\nabla\varphi\right) = S \tag{3.1}$$

where $S(\mathbf{x}, t)$, $\rho(\mathbf{x})$, and $c(\mathbf{x})$ are the source, mass density and sound speed fields, respectively. In the frequency domain this takes the form

$$-\nabla \cdot \left(\frac{1}{\rho}\nabla\hat{\varphi}\right) - \frac{\omega^2}{\rho c^2}\hat{\varphi} = \hat{S}, \tag{3.2}$$

in which Fourier transform pair $\varphi, \hat{\varphi}$ is defined by

$$\begin{aligned} \hat{\varphi}(\mathbf{x}, \omega) &= \int dt \varphi(\mathbf{x}, t) e^{i\omega t} \\ \varphi(\mathbf{x}, t) &= \int \frac{d\omega}{2\pi}\hat{\varphi}(\mathbf{x}, \omega) e^{-i\omega t}, \end{aligned} \tag{3.3}$$

and similarly for S. The formal solution to (3.2) is

$$\hat{\varphi}(\mathbf{x}) = \int d^3x' g(\mathbf{x}, \mathbf{x}')\hat{S}(\mathbf{x}'), \tag{3.4}$$

Distribution A / Approved for public release

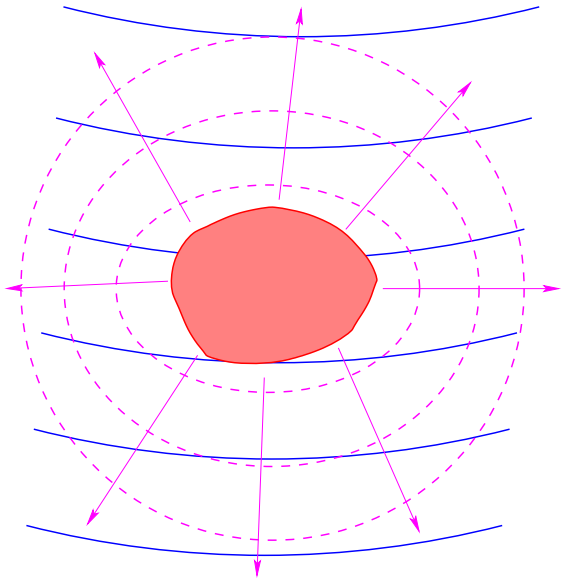

FIG. 3: Schematic illustration of background and scattered (outgoing wave) fields. The former represent the field in the absence of the scatterer, while the latter represent the corrections to the field due to the presence of the scatterer. The two fields are expanded in a set of basis functions according to (3.8) and (3.9), and related via (3.12) through the T-matrix.

in which the Green function g satisfies,

$$\nabla \cdot \left[\frac{1}{\rho}\nabla g(\mathbf{x},\mathbf{x}')\right] + \frac{\omega^2}{\rho c^2} g(\mathbf{x},\mathbf{x}') = -\delta(\mathbf{x}-\mathbf{x}'). \tag{3.5}$$

In an infinite, homogeneous medium, one obtains the free Green function

$$g_0(\mathbf{x}-\mathbf{x}') = \frac{\rho}{4\pi|\mathbf{x}-\mathbf{x}'|} e^{ik|\mathbf{x}-\mathbf{x}'|}, \tag{3.6}$$

with wavenumber $k = \omega/c$.

In general (3.1) will fail if there are non-fluid elements in the medium, such as solid elastic scatterers. However, in what follows we will only require the Green function for the background fluid medium for which (3.1) is valid everywhere.

B. Scattering in a homogeneous background

The so-called T-matrix encodes, for any given frequency, the full scattering responses of a target for all possible incident waves. The T-matrix is most simply defined first for a target lying in an infinite, homogeneous medium, and the definition is then extended to certain classes of inhomogeneous media, including sediment models of interest to the underwater UXO problem.

To describe scattering, the acoustic field is first separated into background and scattered components (see Fig. 3),

$$\hat{\varphi}(\mathbf{x}) = \hat{\varphi}_b(\mathbf{x}) + \hat{\varphi}_s(\mathbf{x}), \tag{3.7}$$

in which, by definition, $\hat{\varphi}_b$ is the field generated by the given source in the absence of the scatterer, and $\hat{\varphi}_s$ corrects for the presence of scattered waves. Let the scatterer be centered on a point $\mathbf{x}_s$ [6]. It is assumed that ϕ_b is smooth and regular in a neighborhood of $\mathbf{x}_s$, including the entire volume occupied by the scatterer, and admits a convergent expansion,

$$\hat{\phi}_b(\mathbf{x}) = \sum_n A_n \xi_n(\mathbf{x}-\mathbf{x}_s) \tag{3.8}$$

in terms of a conveniently chosen set of basis functions $\xi_n(\mathbf{x})$ which are all regular at the origin. Similarly, the scattered field is assumed to admit a convergent expansion,

$$\hat{\phi}_s(\mathbf{x}) = \sum_n B_n \psi_n(\mathbf{x}-\mathbf{x}_s), \tag{3.9}$$

outside a sufficiently large neighborhood of the scatterer. The functions ψ_n will generally be singular somewhere inside this neighborhood. Both sets of basis functions are solutions to the homogeneous acoustic equation (3.2) with $\hat{S} \equiv 0$. For targets that are not too far from spherical, convenient basis function choices are the spherical waves,

$$\begin{aligned} \xi_{lm}(\mathbf{x}) &= j_l(kx) Y_{lm}(\theta,\phi) \\ \psi_{lm}(\mathbf{x}) &= h_l^{(1)}(kx) Y_{lm}(\theta,\phi), \end{aligned} \tag{3.10}$$

in which (x,θ,ϕ) are spherical coordinates for $\mathbf{x}$ centered on the origin, $j_l(z)$ are the spherical Bessel functions (which are indeed regular, varying as z^l near the origin), $h_l^{(1)}(z)$ the spherical Hankel functions (which indeed diverge as $1/z^{l+1}$ at the origin), and Y_{lm} are the spherical harmonics [1].

The T-matrix represents the linear relationship

$$B_n = \sum_{n'} T_{nn'}(k) A_{n'} \tag{3.11}$$

between the A and B coefficients that must emerge from a full solution to the acoustic equation in the presence of the scatterer. For a spherically symmetric scatterer,

$$T_{lm;l'm'}(k) = T_l(k)\delta_{ll'}\delta_{mm'} \tag{3.12}$$

is diagonal and independent of m in the spherical wave basis, and exact solutions are available for a variety of examples. In matrix form, (3.12) is written simply as $\mathbf{B} = \mathbf{TA}$.

Since (3.7)–(3.10) refer only to the solutions in the background medium, the relation (3.12) holds even if the target is, e.g., an elastic body rather than a fluid body. The T-matrix is, of course, much more difficult to compute in such cases.

C. Heterogeneous field T-matrix

Suppose now that the target resides in a medium that is homogenous in the target neighborhood, but not necessarily globally homogeneous. Examples to be discussed

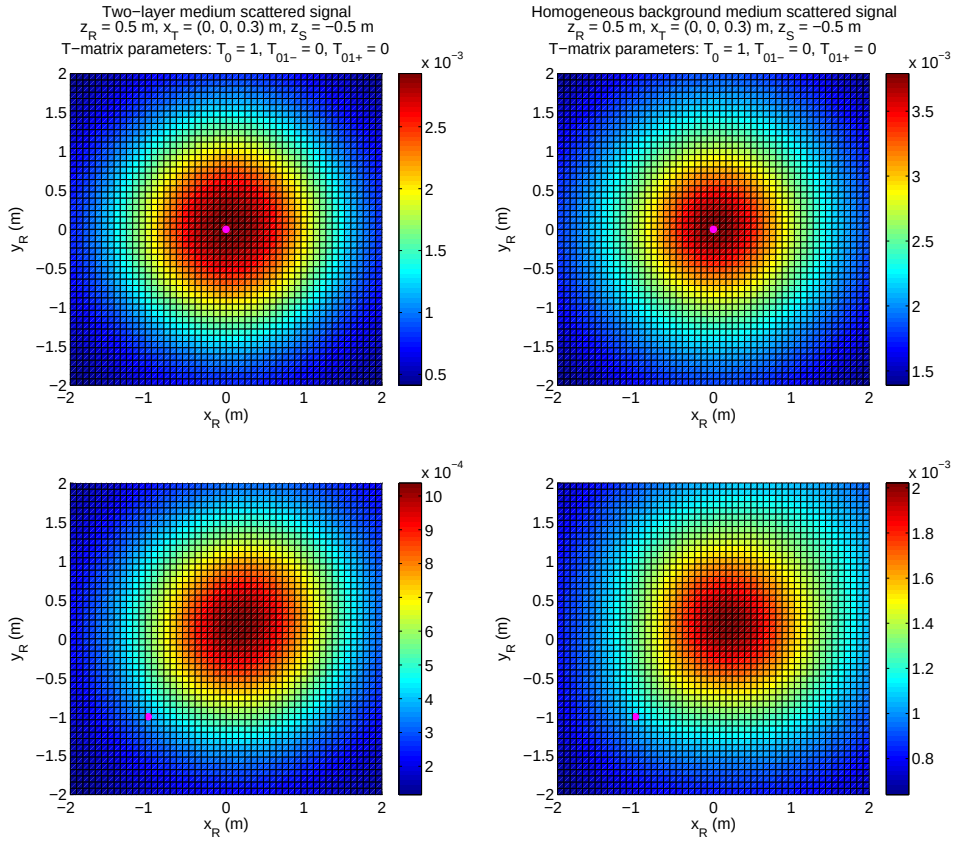

FIG. 4: **Top:** Scattered signal magnitude from a sphere at a single frequency $f = 5$ kHz, modeled by $T_l = T_0/(2l+1)^2$, $0 \leq l \leq 4$, in a homogeneous space (right; parameters $c_1 = 1.5$ km/s, $\rho_1 = 1$ g/cm^3) and buried 0.5 m below the surface in a two layer medium (left; parameters $c_2 = 2.0$ km/s, $\rho_2 = 3$ g/cm^3). In both cases the target lies 0.8 m directly below the horizontally centered transmitter (magenta dot), which in turn lies 0.2 m below the 4 m $\times$ 4 m plane of receiver positions. **Bottom:** Same as above, except that, while the target remains at the horizontal origin, the transmitter is now offset horizontally by 1 m in each direction (magenta dot). The asymmetric transmitter placement induces a similar asymmetry in the scattering intensity pattern. In particular, the signal peak moves in the opposite direction as the transmitter, as would be expected based on a specular reflection picture. In both upper and lower pairs of plots there are quantitative, but not qualitative, changes between left and right.

below include horizontally stratified media, which may or may not contain other compact scatterers. Local homogeneity implies that we may continue to expand the background field (which excludes the effects of the target, but includes the effects of all other inhomogeneities in the medium) locally near $\mathbf{x}_s$ in the form (3.8). However, the scattered field now has an expansion

$$\hat{\phi}_s(\mathbf{x}) = \sum_n B_n \Psi_n(\mathbf{x} - \mathbf{x}_s; \mathbf{x}_s) \tag{3.13}$$

in which Ψ_n is a solution to the global acoustic equation, and the residual $\mathbf{x}_s$ dependence arises because the system is no longer translation invariant. The expansion is uniquely defined by writing, within the local homogeneous neighborhood of the target,

$$\Psi_n(\mathbf{x}; \mathbf{x}_s) = \psi_n(\mathbf{x}) + \Delta\psi_n(\mathbf{x}; \mathbf{x}_s), \tag{3.14}$$

where the correction $\Delta\psi_n$ arises from reflections of the scattered wave ψ_n that return to the neighborhood of $\mathbf{x}_s$. As such, $\Delta\psi_n$ is assumed to be smooth in the neighborhood of $\mathbf{x}_s$, and have a convergent re-expansion,

$$\Delta\psi_n(\mathbf{x}; \mathbf{x}_s) = \sum_{n'} U_{nn'}(\mathbf{x}_s)\xi_{n'}(\mathbf{x}), \tag{3.15}$$

in terms of the regular basis functions. Examples of the matrix $\mathbf{U}$ will be presented below.

The free-field T-matrix now relates the *full* ξ_n component of the field to the scattered field. In matrix form one obtains,

$$\mathbf{B} = \mathbf{T}(\mathbf{A} + \mathbf{U}\mathbf{B}), \tag{3.16}$$

with solution,

$$\mathbf{B} = \mathcal{T}\mathbf{A}, \ \mathcal{T} = (\mathbf{T}^{-1} - \mathbf{U})^{-1}. \tag{3.17}$$

Through (3.17) we have succeeded in expressing the full solution to the scattering problem in terms of the free

Distribution A / Approved for public release

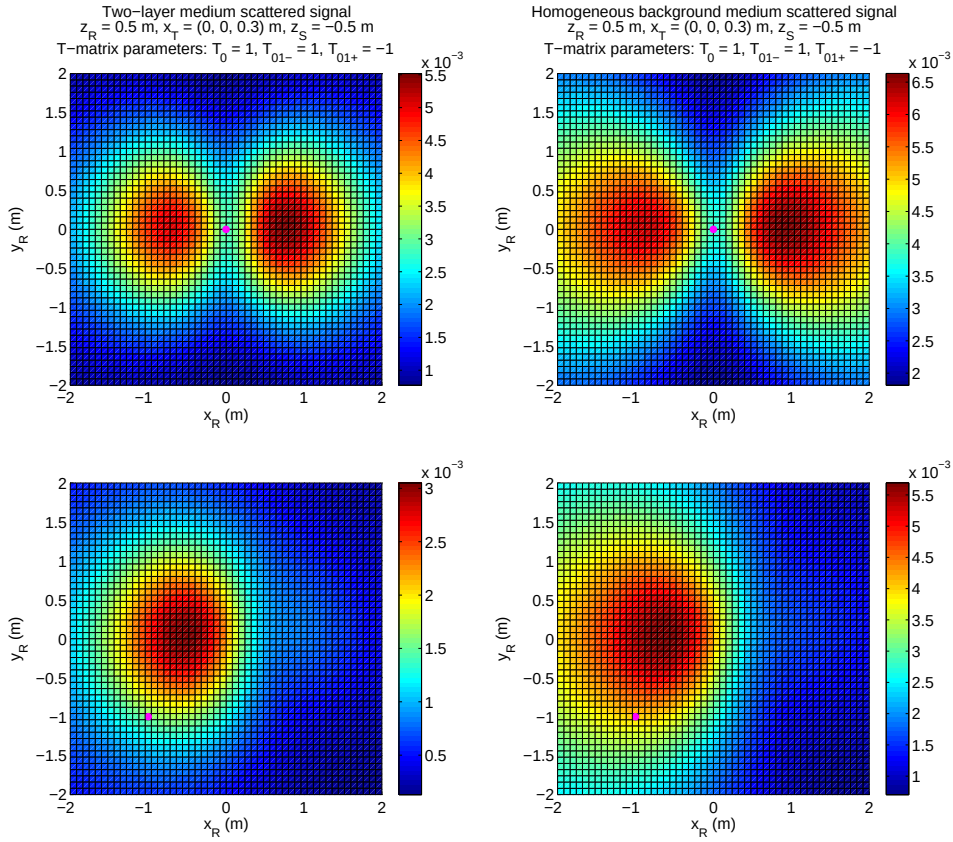

FIG. 5: Same as Fig. 4, except that, in addition to the spherical T-matrix coefficients cited there, one includes nonzero $T_{00;1,-1} = T_{1,-1;00} \equiv T_{01-} = 1$ and $T_{00;11} = T_{11;00} \equiv T_{01+} = -1$. The off-diagonal nature of these coefficients means that they generate an outgoing dipolar wave from a spherically symmetric background wave. The two different transmitter horizontal positions are again shown by the magenta dot.

field scattering problem, together with the global properties of the background medium. The existence of such local scattering relations relies on the spatial locality of the gradients in the acoustic equations (3.1) and (3.2).

It is important to note that the T-matrix will depend on the nature of the background medium via the target-background interaction. For example, buried-target resonant spectra will be different from those of a target in the water column or in air, and this must inform buried-target classification [7].

IV. FORWARD AND INVERSE MODELING OF SCATTERING IN A TWO LAYER SYSTEM

A. Two-layer forms for the scattered signal

In order to illustrate the role that different T-matrix coefficients play in the geometry of the scattered wave, and the distortion induced by transmission through the sediment, we compare here simulations of scattering for targets in free (water-filled) space to those for a target buried in a sediment half space.

For an isotropic point source $S(\mathbf{x}) = S_0\delta(\mathbf{x} - \mathbf{x}_T)$, at position $\mathbf{x}_T$ in the water column, the background field takes the form

$$\hat{\varphi}_b(\mathbf{x}) = \int \frac{d^2q}{(2\pi)^2} e^{\mathbf{q}\cdot(\mathbf{r}-\mathbf{r}_T)} \frac{e^{l_2(q)z - l_1(q)z_T}}{\chi_1(q) + \chi_2(q)}, \tag{4.1}$$

where, here and below, the decomposition $\mathbf{x} = (\mathbf{r}, z)$ of any 3D position denotes horizontal and vertical coordinates, and

$$\begin{aligned} l_u(q) &= \sqrt{q^2 - (\omega/c_u)^2} \\ \chi_u(q) &= l_u/\rho_u, \end{aligned} \tag{4.2}$$

where c_u, ρ_u are sound (phase) speed and mass density in layer $u = 1, 2$. For $q < \omega/c_u$ one defines $l_u = -i\sqrt{(\omega/c_u)^2 - q^2} \equiv -iq_{z,u}$.

By expanding (4.1) in the spherical harmonic basis functions (3.10), the A-coefficients may be reduced to

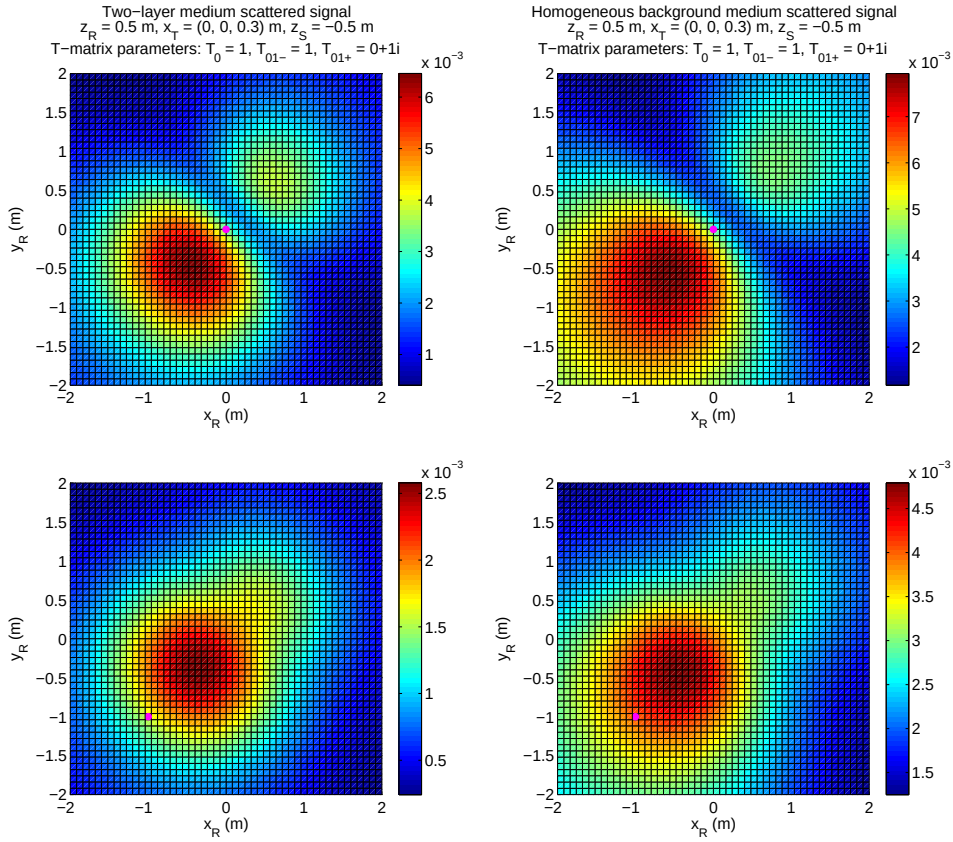

FIG. 6: Same as Fig. 5, except that the values $T_{01-} = 1$ and $T_{01+} = i$ are used. Altering the magnitude and phase of these coefficients is seen to rotate the pattern, and change the balance between the two lobes. The two different transmitter horizontal positions are again shown by the magenta dot.

the 1D integrals

$$A_{lm} = 2i^{l-m} S_0 \beta_{lm} e^{-im\phi^{(TS)}} \int_0^\infty q dq J_m(q|\mathbf{r}_T - \mathbf{r}_S|) \times P_l^m[-\sqrt{1-(c_2 q/\omega)^2}] \frac{e^{l_2(q)z_S - l_1(q)z_T}}{\chi_1(q)+\chi_2(q)}, \tag{4.3}$$

where $\mathbf{x}_S$ is the scatterer position, $\phi^{(TS)}$ is the horizontal plane azimuthal angle associated with $\mathbf{r}_T - \mathbf{r}_S$, $\beta_{lm} = \sqrt{(2l+1)(l-m)!/4\pi(l+m)!}$, $J_m(z)$ is the usual cylindrical Bessel function, and $P_l^m(x)$ are the associated Legendre functions [8].

The U-matrix is given by a corresponding 1D integral,

$$U_{lm;l'm'} = i^{l-l'-m} \delta_{mm'} \beta_{lm} \beta_{l'm} \frac{4\pi c_2}{\omega \rho_2} \int_0^\infty q dq e^{2l_2(q)z_S} \times P_l^m[-\sqrt{1-(c_2 q/\omega)^2}] P_{l'}^m[\sqrt{1-(c_2 q/\omega)^2}] \times \frac{\chi_1(q)+\chi_2(q)}{\chi_2(q)[\chi_1(q)+\chi_2(q)]}, \tag{4.4}$$

which depends only on the scatterer vertical coordinate z_S, and is diagonal in m, m'.

For a given T-matrix, the (scattered wave) B-coefficients may now be computed from (3.17). Finally, given these coefficients, an isotropic point receiver $R(\mathbf{x}) = R_0 \delta(\mathbf{x} - \mathbf{x}_R)$ will receive a signal in the form of the sum (3.13)

$$\hat{\varphi}_R = R_0 \sum_{l,m} B_{lm} \hat{\varphi}_{R,lm} \tag{4.5}$$

in which the scattered wave basis functions evaluated at the receiver position $\mathbf{x}_R$ are given by the 1D integral

$$\hat{\varphi}_{R,lm} = i^{m-l-1} \frac{2c_2}{\omega \rho_2} \beta_{lm} e^{im\phi^{(RS)}} \int_0^\infty q dq J_m(q|\mathbf{r}_R - \mathbf{r}_S|) \times P_l^m[\sqrt{1-(c_2 q/\omega)^2}] \frac{e^{l_2(q)z_S - l_1(q)z_R}}{\chi_1(q)+\chi_2(q)}, \tag{4.6}$$

where $\phi^{(RS)}$ is the horizontal plane azimuthal angle associated with $\mathbf{r}_R - \mathbf{r}_S$.

For comparisons below, in free space one obtains the fully analytic forms

$$A_{lm} = i \frac{\rho_1 \omega}{c_1} h_l^{(1)} \left(\frac{\omega}{c_1} |\mathbf{x}_S - \mathbf{x}_T| \right) Y_{lm}^*(\theta^{(TS)}, \phi^{(TS)})$$
$$\hat{\varphi}_{R,lm} = h_l^{(1)} \left(\frac{\omega}{c_1} |\mathbf{x}_R - \mathbf{x}_S| \right) Y_{lm}(\theta^{(RS)}, \phi^{(RS)}), \tag{4.7}$$

where $h_l^{(1)}(z)$ is the spherical Hankel function [8], $\theta^{(TS)}, \phi^{(TS)}$ are the polar coordinate angles associated with $\mathbf{x}_T - \mathbf{x}_S$, and $\theta^{(RS)}, \phi^{(RS)}$ are the polar coordinate angles associated with $\mathbf{x}_R - \mathbf{x}_S$. The received signal is still given by (4.5), but now with the direct relationship $\mathbf{B} = \mathbf{TA}$ replacing (3.16) and (3.17).

B. Examples of computed scattering returns

In Figs. 4–6 we show two-layer and free-space forms (with medium parameters described in the caption to Fig. 4) for the magnitude of the scattered signal, obtained via numerical implementation of (4.3)–(4.7). The signal is sampled (for a single fixed frequency) on a 4 m × 4 m horizontal grid 1 m above the sediment, for various choices of T-matrix parameters. The transmitter is 0.2 m below this grid, and we compare results for two different horizontal locations.

Fig. 4 shows results for a spherical target. The T-matrix takes the form (3.12) with the (somewhat arbitrary) choice $T_l = T_0/(2l+1)^2$, $0 \le l \le 4$, and $T_l = 0$ for $l \ge 5$. The homogeneous vs. two-layer signals are qualitatively similar, but clearly differ quantitatively. Accurate inference of T-matrix parameters (see below) therefore requires proper modeling of the sediment.

Figs. 5 and 6 illustrate the role of "off-diagonal" T-matrix coefficients, specifically those that couple $l = 0$ (spherically symmetric) and $l = 1$ (dipolar symmetry) waves. The coefficients $T_{00;1,\pm1}$ and $T_{1,\pm1;00}$ are seen to give rise to a horizontal dipole pattern, with their relative magnitude and phase determining the orientation and relative intensity of the two lobes. The coefficients $T_{00;10}$ and $T_{10;00}$, if present, would control the vertical component of the dipole. Notice that, depending on the transmitter position, one of the lobes can essentially disappear, and the aspherical character of the target could be missed. This points again to the need for a wide diversity of transmitter and receiver positions for robust target characterization.

C. Simulated T-matrix inversions from bistatic measurements

In Sec. II we discussed extraction of sediment acoustic propagation properties from reflection data. Here we will assume, from such a prior inversion procedure, that the sediment model is known (we use physically reasonable values $c = 1.5$ km/s, $c_2 = 1.7$ km/s, $\rho_1 = 1$ g/cm^3, $\rho_2 = 1.9$ g/cm^3, and frequency $f = 5$ kHz throughout), and use it to investigate inversion of T-matrix parameters. We will focus in particular on the influence of transmitter–receiver diversity and inversion accuracy.

The inversions are performed by minimizing the simple

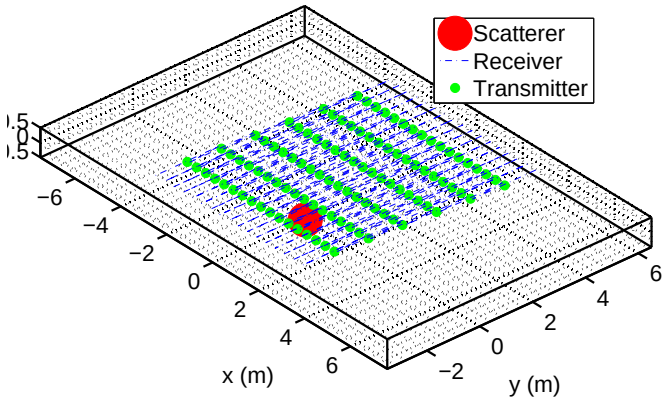

FIG. 7: Oblique view of a notional BOSS data collection geometry, showing five tracks separated by $\Delta y = 1.2$ m, with data taken every $\Delta x = 0.4$ m. The blue dashed lines indicate the 2.4 m span of the BOSS receiver wings.

mean-squared error functional,

$$E(\mathbf{T}, \mathbf{x}_S, \mathbf{M}) = \sum_{i=1}^{N_R} \sum_{j=1}^{N_T} [\hat{\varphi}_{\text{meas}}(\mathbf{x}_{R,i}, \mathbf{x}_{T,j}) - \hat{\varphi}_{\text{pred}}(\mathbf{x}_{R,i}, \mathbf{x}_{T,j})]^2 , \quad (4.8)$$

which depends on the target position $\mathbf{x}_S$, the T-matrix parameters $\mathbf{T}$, and the background medium parameters $\mathbf{M}$ through the predicted received waveform $\hat{\varphi}_{\text{pred}}$ (computed as described in Sec. IV A).

To obtain sufficient data to extract individual T-matrix coefficients, one requires a set of bistatic measurements, with angular diversity sufficient to explore a broad range of scattering angles θ. A notional measurement protocol is shown in Fig. 7, in which the platform (with transmitter at the center, and 20 receivers spaced uniformly along each wing) sweeps an area with track separation $\Delta y = 1.6$ m and data taken at spacing $\Delta x = 0.4$ m along each track. This type of search pattern would be typical of an area scan without prior knowledge of target location.

We begin by considering a single pass over the target, as illustrated in the top panel of Fig. 8. We have found that even using an extremely low platform height of 0.5 m above the sediment (with 0.5 m target depth), the centered transmitter gives very poor inversion results. In this figure, therefore, we instead place the transmitter on one of the wingtips, effectively doubling the bistatic angular aperture. The inversion results, shown in the bottom panel of this figure, are far from perfect, but at least one sees some correlation between truth and estimate. The results are also found to degrade strongly at more realistic platform heights, say 2 m above sediment.

In Fig. 9, using the same modified BOSS geometry, we show the drastic improvement obtained using multiple tracks (with geometry illustrated in the top panel). Even though the transmitter-receiver separation is always con-

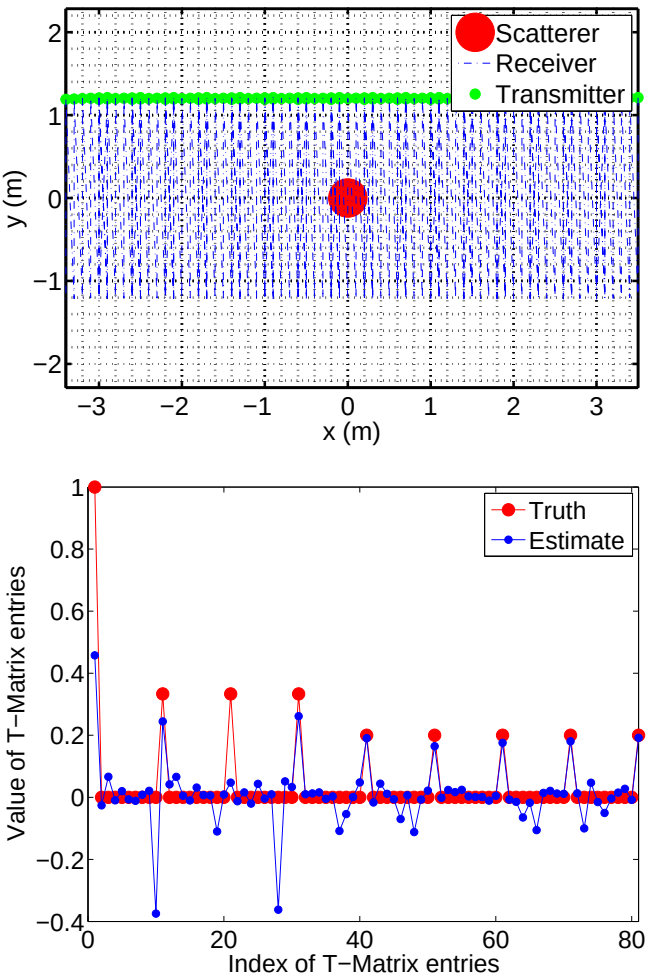

FIG. 8: Simulated T-matrix inversion results (bottom) using a single pass of a modified BOSS with a wingtip transmitter to enhance the bistatic angular diversity (top). The target is centered 0.5 m below the sediment surface, while the BOSS platform is centered at 0.5 m above it, and the along-track spacing is $\Delta x = 0.1$ m. A signal-to-noise ratio (SNR) level of 30 dB was used. It is clear that even with this enhanced angular coverage, the inversion results are mediocre at best.

strained to be less than 2.6 m, different T-matrix coefficients are sensitive to different "view" angles of the target. The combination of wide aperture and different views provided by the multiple tracks (and the overlapping quality of the tracks, relative to the BOSS wingspan, was also found to be important here) produce decent inversions even at 2 m platform height (center panel of the figure). A platform height of 0.5 m produces essentially perfect inversions (lower panel).

It should be noted that a newer version of the BOSS platform has a 4 m wingspan, and the results above are therefore consistent with a centered transmitter on this platform. Doubling the aperture to 4 m by placing the transmitter on the wingtip should provide an even greater enhancement, even for the single-pass results (Fig. 8).

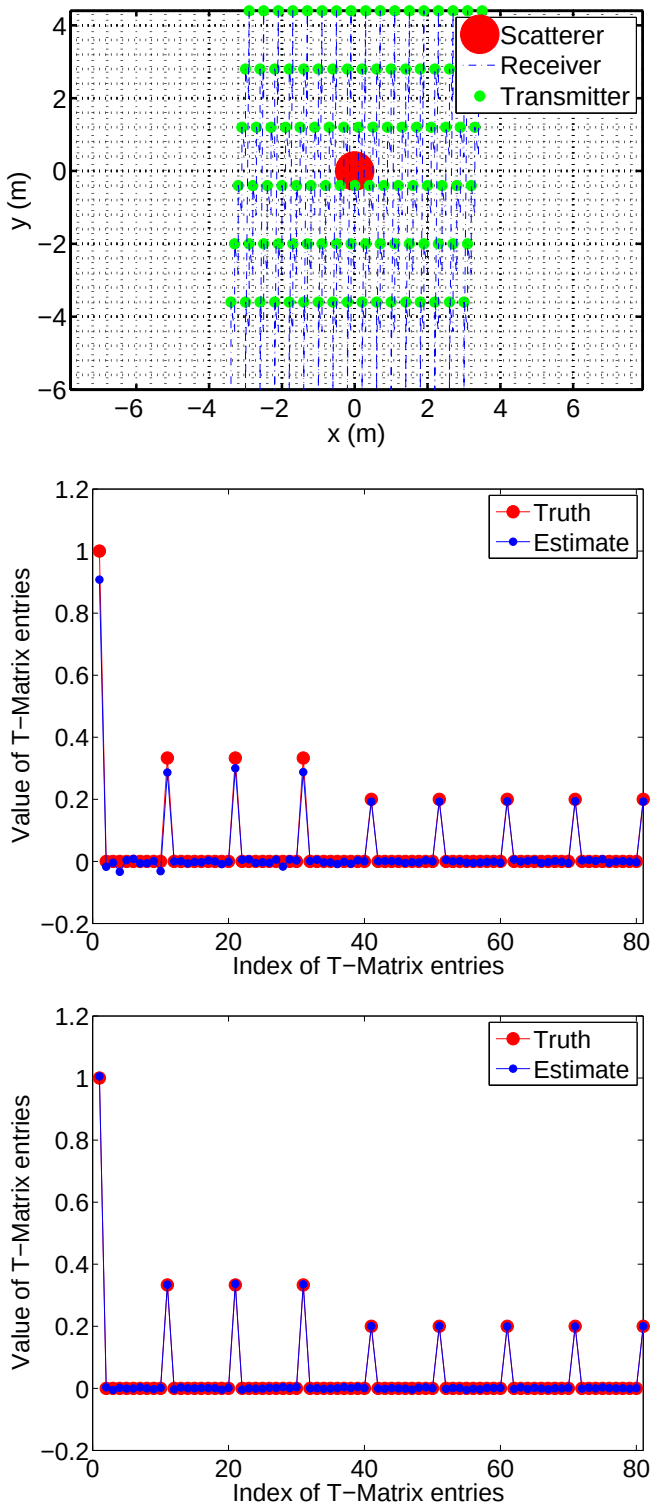

FIG. 9: Simulated T-matrix inversion results using six passes, with $\Delta x = 0.4$ m along-track spacing between measurements, of a modified BOSS with a wingtip transmitter to enhance the bistatic angular diversity (top). For the center plot, the target is centered 0.5 m below the sediment surface, while the BOSS platform is centered at 2 m above it. Moderate inversion accuracy is seen. For the bottom plot the platform is lowered to 0.5 m above the surface, and essentially perfect inversion accuracy is seen. A SNR level of 30 dB was used in both cases.

Distribution A / Approved for public release

This will be explored in greater detail in the near future.

V. ACOUSTIC DATA ANALYSIS BACKGROUND: PULSE COMPRESSION

To avoid propagation nonlinearities (cavitation, in extreme cases) in the propagation, acoustic pulses, or pings, are sent out as long chirps, as opposed to sharp, high amplitude pings:

$$S(t) = A(t)e^{i\phi(t)} \tag{5.1}$$

in which the frequency is usually a linear ramp over a frequency band $\omega_{\min} \leq \omega \leq \omega_{\max}$:

$$\begin{aligned} \phi(t) &= \omega_{\min} t + \frac{1}{2} K \omega t^2 \\ K &= \frac{\omega_{\max} - \omega_{\min}}{T}, \end{aligned} \tag{5.2}$$

where $T \gg 2\pi/\omega_{\min}$ is the length of the chirp, encompassing many cycles. For large T, the local frequency

$$\omega(t) \equiv \partial_t \phi(t) = \omega_{\min} + Kt, \tag{5.3}$$

varies slowly in time, and the chirp may be thought of as probing the medium at a series of frequencies. The amplitude $A(t)$ is smooth, turning on smoothly near the edges of the band, and acts as a window on the band. The pulse spectrum

$$\hat{S}(\omega) = \int dt e^{i\omega t} S(t) \tag{5.4}$$

has magnitude

$$\hat{A}(\omega) = |\hat{S}(\omega)| \propto A\left(\frac{\omega - \omega_{\min}}{K}\right) \tag{5.5}$$

that is a very similarly shaped window supported on the band $[\omega_{\min}, \omega_{\max}]$.

Typical parameters for the BOSS platform are $f_{\min} =$ 3 kHz, $f_{\max} = 22$ kHz over $T = 6.4$ ms, so that the chirp contains $(f_{\min} + f_{\max})T/2 = 80$ cycles. The window $A(t)$ is a linear ramp for the first and last 5% of the chirp, and flat in between.

For the NSWC PCD scale tank, $f_{\min} = 200$ kHz, $f_{\max} = 900$ kHz over $T = 0.36$ ms, so that the chirp contains 200 cycles. The amplitude $A(t)$ takes the form of a $\cos^2$ envelope, turning on and off as $\sin^2(\pi s/2t_0)$, $0 \leq s \leq t_0 \simeq 0.07$ ms, where s is the time difference from the chirp endpoints, and is flat in between.

If one models the received signal as a superposition of scattered pings,

$$\varphi(t) = \int_0^{ct/2} dr f(r) S(t - 2r/c) \tag{5.6}$$

where $f(r)$ is the amplitude of the scattering from the medium at range r, then the signal at time t will be a superposition of time delayed chirps from a broad set of ranges spanning a distance $cT/2$. In order to isolate different returns, one performs the pulse compression operation using the chirp complex conjugate,

$$\begin{aligned} \varphi_c(t) &= \int_0^T dt' S(t')^* \varphi(t + t') \\ &= \int dr f(r) S_c(t - 2r/c), \end{aligned} \tag{5.7}$$

where the compressed pulse

$$S_c(t) = \int \frac{d\omega}{2\pi} e^{-i\omega t} |\hat{A}(\omega)|^2 \tag{5.8}$$

has minimal width $\Delta t \approx 2\pi/(\omega_{\max} - \omega_{\min})$ approaching the Heisenberg limit. As long as targets are well separated on the range scale $c\Delta t/2$, their returns will appear in (5.7) as isolated pulses. Thus, the combination of pulse compression and time windowing allows one to isolated individual returns. The spectra of these windowed returns may then be computed, thereby isolating the spectral responses (scattering amplitude vs. frequency) of individual targets.

Note that an approach, alternative to chirps, would be a stepped frequency source, with longer dwell time on each frequency. This would likely produce lower SNR data through time averaging at each frequency. However sonar platforms are generally moving too quickly relative to the signal propagation speed to make this approach sensible, and chirps become the best available option.

VI. DATA ANALYSIS: FREE-FIELD SPHERE BOSS DATA

A. Pulse compression and beam forming

As our first example of pulse compression processing, Fig. 10 shows the magnitude of the raw return (5.6) at a single receiver for a series of 150 chirps launched by the BOSS platform. The pulse origins are spaced by about 4 cm through the linear motion of the platform. The bottom return forms the major part of the scattered signal, with scattering from the target of interest (a 4" diameter sphere, at $d = 2.7$ m offset at closest approach) appearing only as a weak ripple on top of this.

The result of the pulse compression operation is dramatically different, and is shown in Fig. 11. The narrow sphere return is now well separated from the bottom return, corresponding to about 5.3 m depth. As shown in Fig. 12, a fit to the hyperbolic arc

$$t_m = \frac{1}{c}\sqrt{d^2 + (\Delta x_m)^2}, \tag{6.1}$$

where t_m is the time delay of ping m, and Δx_m is the along-track distance from closest approach, is indeed consistent with the above standoff and ping separation.

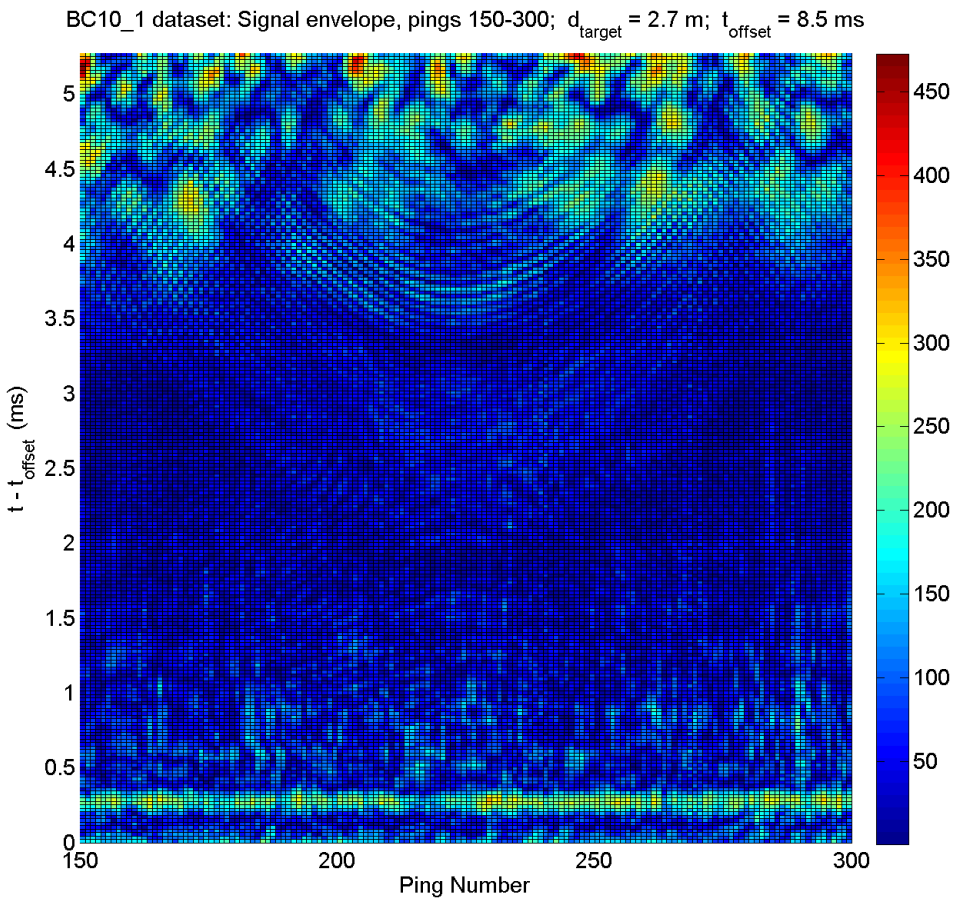

FIG. 10: Time-domain back-projection image formed from signal envelope time traces for a series of 150 pings separated by 4 cm. In this unprocessed image, the scattering return from a 4-in diameter sphere at 2.7 m offset appears as a weak ripple on the bottom-reflection background.

To increase SNR, we now perform the beam-forming operation

$$\varphi_{\mathrm{c,beam}}(t) = \sum_{m=1}^{N_p} \varphi_{c,m}(t - t_m), \tag{6.2}$$

where N_p is the number of pings used. The time delay is designed to line up all of the returns in phase. For a spherical target, these returns should all be identical (up to a $1/r$ geometric spreading factor), and the sum should therefore increase SNR by a factor of order $\sqrt{N_p}$. The resulting (compressed, beam-formed) waveform is shown in the upper panel of Fig. 13.

B. Backscattering spectrum

The lower panel of Fig. 13 shows the resulting spectrum, along with the chirp spectral window function (5.5). In order to interpret this spectrum, in relation to the T-matrix coefficients, one makes use of the plane wave decomposition

$$e^{i\mathbf{k}\cdot\mathbf{x}} = \sum_l i^l (2l+1) j_l(kx) P_l[\cos(\theta)], \tag{6.3}$$

where $\cos(\theta) = \hat{\mathbf{k}} \cdot \hat{\mathbf{r}}$ and $P_l(x)$ are the Legendre polynomials. Using the far field expansion (which is well obeyed in this experiment) of the spherical Hankel function,

$$h_l(x) \approx (-i)^l \frac{e^{ix}}{ix}, \tag{6.4}$$

it follows from the basis function representations presented in Sec. III that the scattered field generated by an incident plane wave takes the form of an outgoing spherical wave

$$\hat{\varphi}(\mathbf{x}) \approx f(\hat{\mathbf{r}}; \mathbf{k}) \frac{e^{ikr}}{r} \tag{6.5}$$

where f is the scattering amplitude, and the unit vector $\hat{\mathbf{r}}$ defines the observation direction $\mathbf{r} = \mathbf{x} - \mathbf{x}_S$. For a spherically symmetric scatterer, one obtains from (3.12)

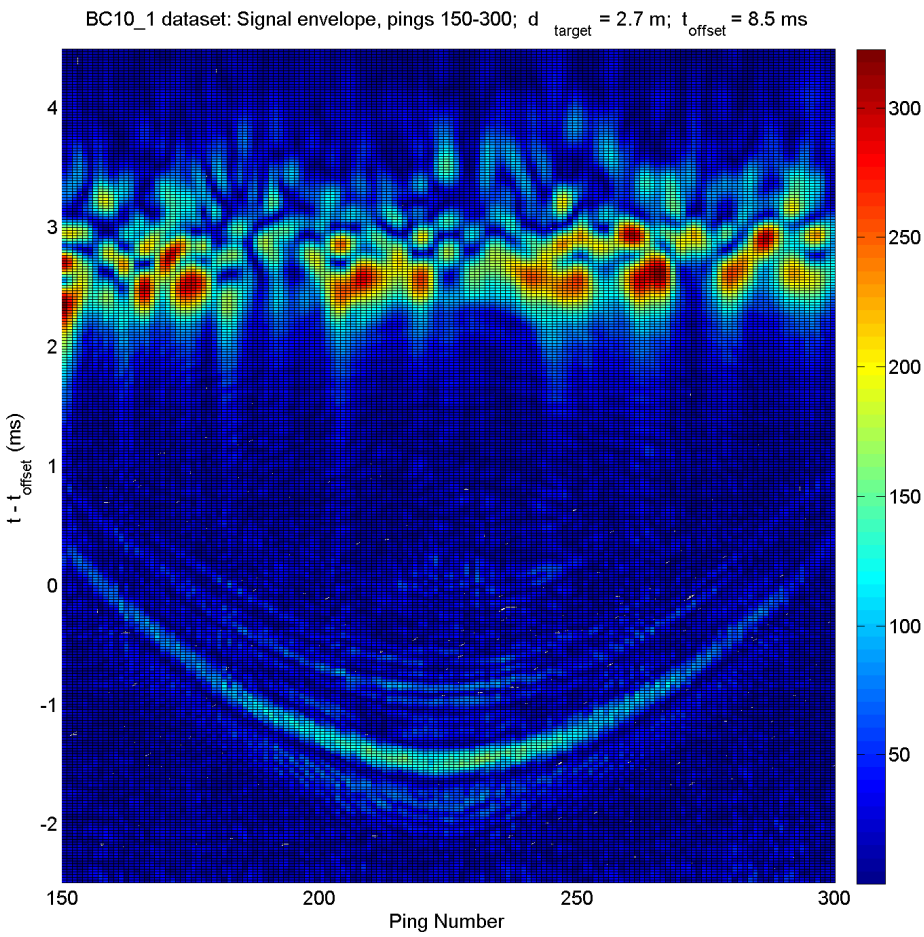

FIG. 11: Same as Fig. 10 but plotted now are the signal envelope time traces after the pulse compression operation has been applied. The scattered signal from the sphere is now completely separated from the bottom reflection. Note that the compression operation, which may be thought of as separately adjusting the time of flight for each frequency component, thereby causes the time range to shift from that in Fig. 10.

the relation

$$f(\hat{\mathbf{r}};\mathbf{k}) = \frac{1}{ik}\sum_l (2l+1)T_l(k)P_l[\cos(\theta)], \tag{6.6}$$

which also depends only on the relative angle θ of the incident and outgoing directions. Now, for a backscatter measurement, $\hat{\mathbf{r}} = -\hat{\mathbf{k}}$, one obtains

$$f(-\hat{\mathbf{k}};\mathbf{k}) = \frac{1}{ik}\sum_l (-1)^l(2l+1)T_l(k), \tag{6.7}$$

representing therefore a single linear combination of T-matrix coefficients for each frequency $\omega = ck$. This is the function shown in the lower panel of Fig. 13, and it is therefore seen that it is impossible to extract individual coefficients from a backscatter measurement alone.

For a nonspherical scatterer (6.6) is replaced by

$$f(\hat{\mathbf{r}};\mathbf{k}) = \frac{1}{ik}\sum_{l,m} f_{lm}(\mathbf{k})Y_{lm}(\theta,\phi), \tag{6.8}$$

where θ, ϕ are the orientation angles corresponding to $\hat{\mathbf{r}}$. This form allows for a non-axially symmetric scattered wave. Here $f_{lm}(\mathbf{k})$ represents a certain weighted sum of the $T_{lm;l'm'}(k)$ over l', m' that depends on the incident wave direction. For a backscatter measurement $\hat{\mathbf{r}} = -\hat{\mathbf{k}}$ one again obtains a single linear combination of all the T-matrix coefficients for a given $\mathbf{k}$. Multiple backscatter measurements for different $\mathbf{k}$ produce different linear combinations, but this provides at best (for full 4π angular coverage) only a 2D projection of the full four-dimensional set of coefficients defined by $l, m, l'm'$. Individual coefficients are again impossible to to extract.

We have also analyzed data for multiple receivers and find that the angular diversity is insufficient to distinguish the different returns from pure backscatter at this standoff. In Sec. IV C we described simulated inversion results using much closer approaches, and more diverse sets bistatic measurements, and found that the geometric requirements for robust inversion are quite stringent. Specifically, one needs angular diversity sufficient to ex-

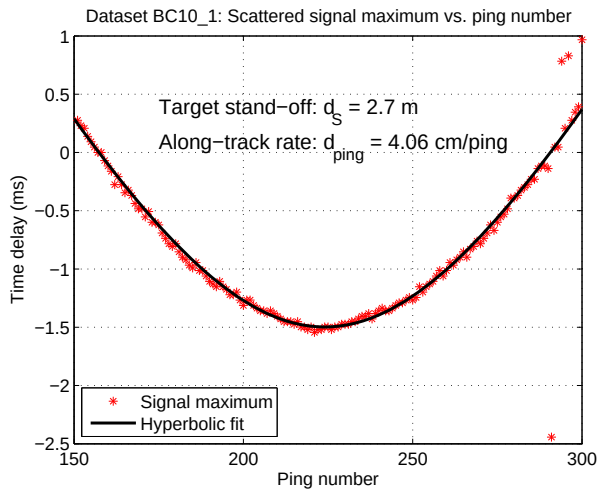

FIG. 12: Hyperbolic fit to the sphere return in Fig. 11. The red stars show the time bin for the signal maximum in each time trace. The fit yields a 2.7 m standoff and 4.06 cm spacing between pings, which accords well with the ground truth.

plore a broad range of $\cos(\theta)$ in (6.6). A newer, NSF–sponsored BOSS platform having a 4 m wingspan, might provide sufficient angular aperture for low enough passes. This will be explored in more detail in the near future.

VII. DATA ANALYSIS: SCALE-TANK MEASUREMENTS ON SPHERICAL AND CYLINDRICAL TARGETS

In order to demonstrate experimentally the added benefit that can be obtained from bistatic data, we discuss briefly here a set of NSWC high quality laboratory scale tank data using $\frac{3}{16}''$ diameter aluminum sphere as a target. The geometry and parameters of the measurements are shown in Fig. 14. Figure 15 shows the backscatter data from receiver R_1, while Fig. 16 shows the bistatic scatter data from receiver R_2. In both cases, the receiver angle refers to the simultaneously rotating position of R_2, and the orientation of the target. The upper panel each figure shows the compressed pulse, indicating the microsecond level accuracy with which the acoustic propagation time can be determined. The lower panel shows the pulse spectrum.

In Fig. 15 the pulse spectrum changes very little with angle, consistent with the invariance of the backscatter with sphere orientation. This confirms as well that there is essentially no T-matrix coefficient information in this data.

On the other hand, in Fig. 16 one sees very interesting variation of the scattering amplitude with frequency and angle. The angular variation becomes less pronounced at lower frequency, consistent with a more rapid vanishing of the higher order $T_l(k)$. Figure 17 shows the results of

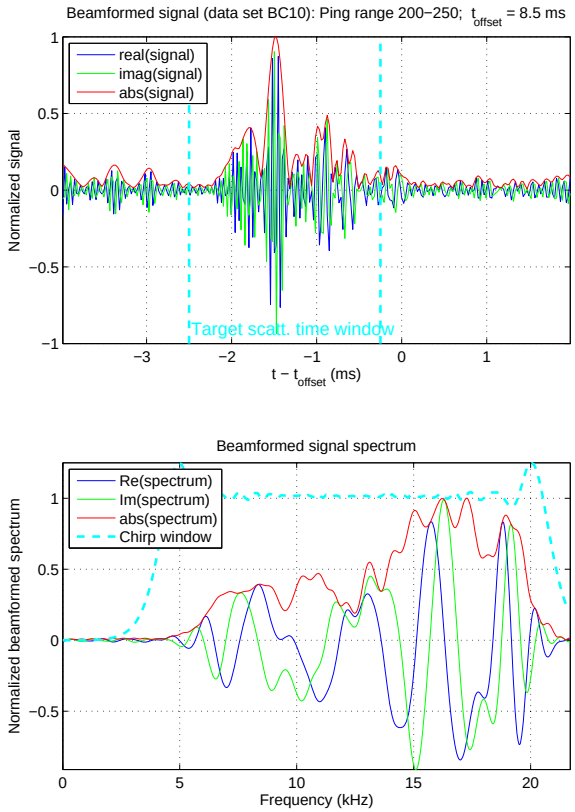

FIG. 13: **Top:** Beam-formed, pulse-compressed time trace, formed from $N_p = 51$ pings (numbered 200–250 in Fig. 11) using the time delays generated by the hyperbolic fit in Fig. 12. The vertical dashed lines show the time window of the return that will be used to generate the scattered spectrum. The 43.4 kHz sampling rate means that there are only about 100 time bins in this window. **Bottom:** Spectrum obtained from the Fourier transform of the of the windowed time trace. The dashed line shows the normalized frequency window $\hat{A}(\omega)$ generated by the pulse compression operation. At low frequency, $a/\lambda \ll 1$, where $a = 5$ cm is the sphere radius, theory predicts $T_0 \propto (a/\lambda)^2$, and $T_l \propto (a/\lambda)^{l+1}$ for $l \geq 1$. Thus, $T_0, T_1 \propto f^2$ dominate at low frequency. For $5 \leq f \leq 20$ kHz one has $0.17 \leq a/\lambda \leq 0.67$. The spectrum indeed displays this expected trend of increasing backscatter with frequency, but is difficult to interpret beyond this.

an optimal fit of the data to the series

$$f(\theta, \omega) = \sum_{l=0}^{l_{\max}} A_l(k) P_l[\cos(\theta)] \tag{7.1}$$

using maximum Legendre polynomial index $l_{\max} = 9$. Here, comparing (6.6), one identifies $A_l(k) = (2l + 1)T_l(k)/ik$. In Figs. 18 and 19 we compare this finite series to the data, first at the single frequency $f = 500$ kHz, and then over all frequencies. The results confirm a poorer fit at higher frequencies, where rapid variation

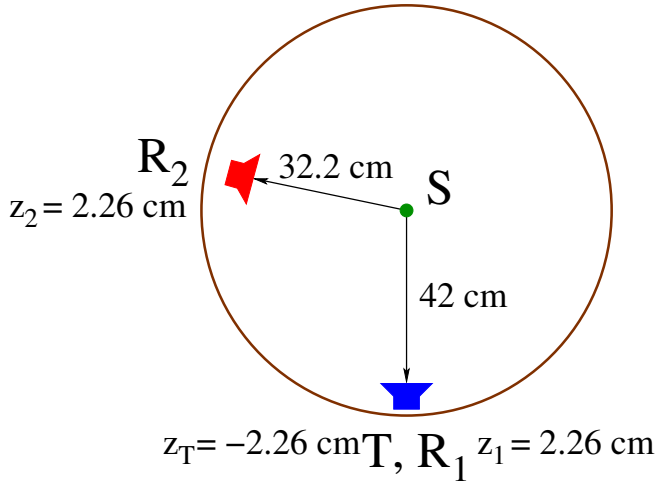

FIG. 14: NSWC scale tank geometry. The target S is centered at the origin. Relative to this, the 1″ transmitter element T is at radius 42 cm and height −2.26 cm, and the 1″ backscatter receiver R_1 is directly above it at height +2.26 cm. The 1″ "forward scatter" receiver R_2 moves on a track of radius 32.2 cm, also at height +2.26 cm. In the data we describe, the transmitted linear chirps span the band 200–900 kHz (wavelengths from 7.5 mm to 1.6 mm), and have a $\cos^2$ envelope. As the second receiver rotates, the target rotates along with it.

in the scattering amplitude is evident especially as one approaches forward angle scattering, which is likely due to shadowing effects.

We have developed codes that implement the exact analytic solutions for scattering from an elastic sphere. We have not yet validated these codes with the data shown in this figure, but will do so in immediate future work.

The essential takeaway from this brief introduction to the tank data is that transmitter-receiver angular diversity is critical to recovering T-matrix information. It is seen, for example, that the interesting spectral variations seen in Fig. 16 really only begin to manifest strongly beyond about 45°.

VIII. CONCLUSIONS

The results described in this document support the following major conclusions:

1. Bistatic measurements, specifically with a diverse set of incident and reflection angles enabled by large measurement aperture, will enable large gains in key parameter estimation.

   (a) Absent large angular aperture, one is mainly measuring the backscatter amplitude and, as described in Sec. VI B, this does not contain enough information to usefully resolve T-matrix coefficients.

   (b) *BOSS utility:* We have verified through simulation that the newer 4 m wingspan BOSS platform, flown at sufficiently low altitude, could provide the necessary aperture, but this needs to be validated through near-future focused data collects. A simple way of essentially doubling the aperture would be to place *additional transmitters at the wing tips* [**?**].

   (c) *Bottom sediment acoustic properties:* there will be huge gains in inverting the angle-dependent reflection coefficient $R(\theta)$ for sediment sound speed and density if one is able to approach the critical angle θ_c. The attached document, which details our attempts to use BOSS datasets to infer bottom sediment properties, shows that the required data sets do not yet exist, but they are within reach of a low-flying 4 m BOSS.

   (d) *T-matrix coefficients and target discrimination:* As stated earlier, our aim is to correlate scattered wave geometry (i.e., multipole structure of the outgoing wavefront) with target internal characteristics (e.g., aspect ratio, identification of vibrational modes). As illustrated, especially by the scale tank data, this multipole structure can only be accessed robustly with large aperture. Again, a low-flying 4 m BOSS, especially one with wingtip transmitters, may be sufficient. However, this needs to be validated with real data.

2. *Looking to the near and further future:* Once the basic utility of T-matrix-derived features is demonstrated, one can imagine various enhanced data collection platforms and strategies to support their extraction.

   (a) *Enhanced BOSS:* As suggested above, the simplest proposal would be to add wingtip trans-

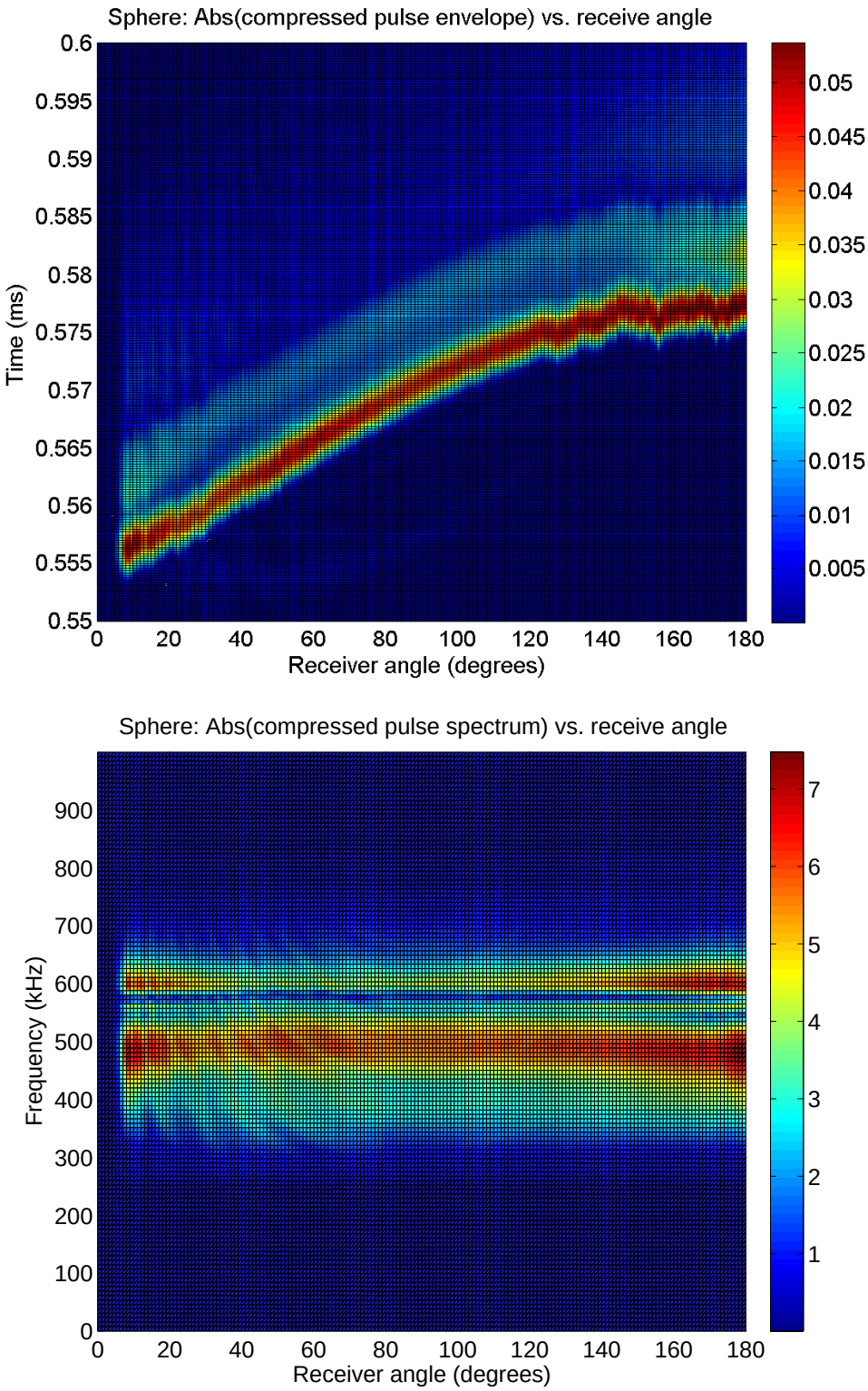

FIG. 15: **Top:** Pulse compressed backscattered returns (receiver R_1 in Fig. 14) for a suspended $\frac{3}{16}''$ diameter aluminum sphere. **Bottom:** Backscattered return spectrum. The transmitter and receiver are fixed, but the target rotates by 180° (along with receiver R_2). In a perfect measurement on a perfect sphere, there should be no variation with angle. The roughly 0.02 ms variation in arrival time corresponds to a 3 cm change in acoustic path length. To within experimental tolerance, however, the spectra are consistently uniform in angle.

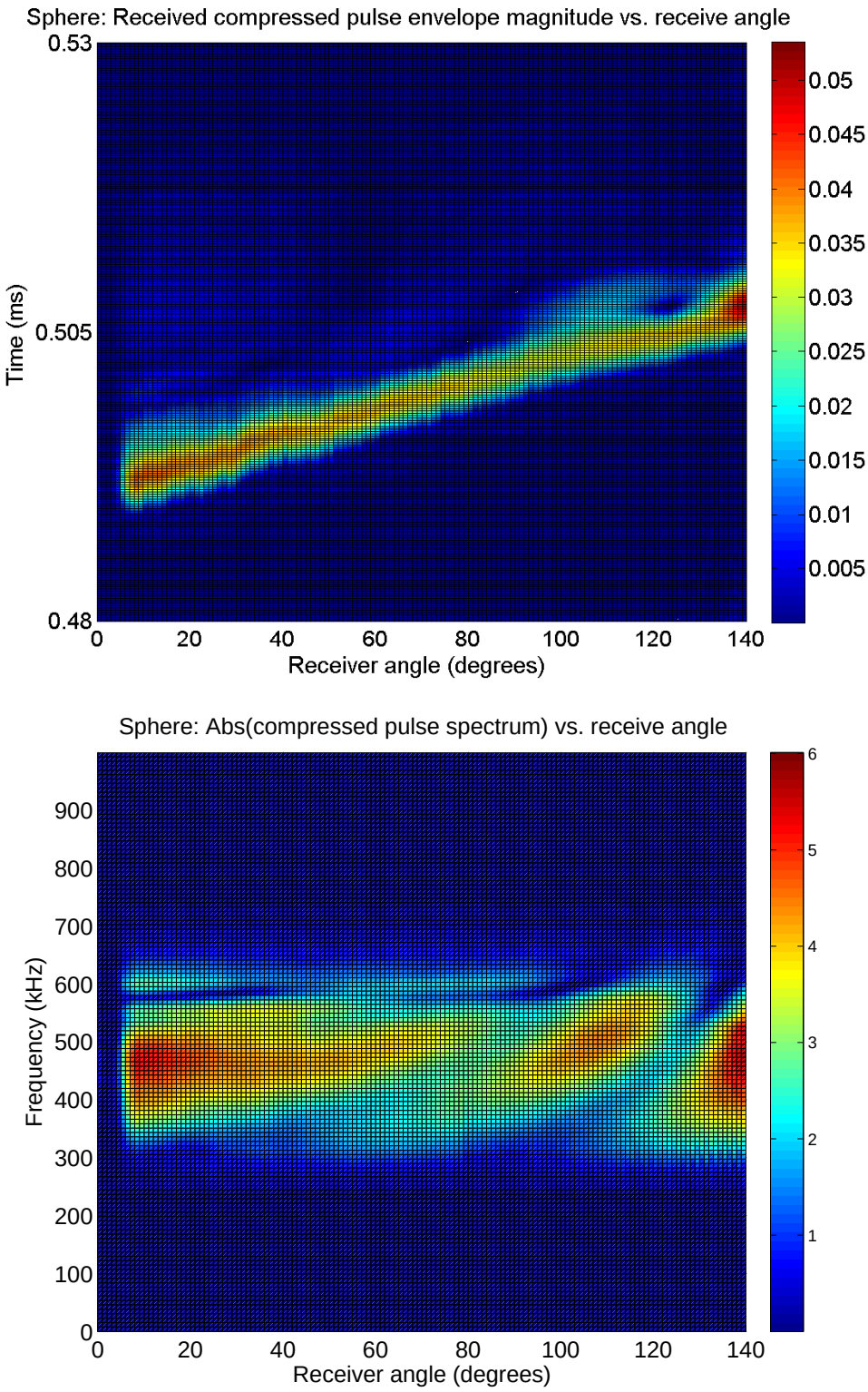

FIG. 16: **Top:** Pulse compressed bistatic scattered returns (receiver R_2 in Fig. 14) for a suspended $\frac{3}{16}$-in diameter aluminum sphere, taken during the same run as the backscatter data in Fig. 15. The 140° angle range is reduced here from 180° because the much brighter direct path begins to dominate the signal. **Bottom:** Bistatic scattered return spectrum. In a perfect experiment the pulse arrival times should be independent of angle; the roughly 0.015 ms variation in arrival time corresponds to a 2 cm change in acoustic path length. The spectra, however, which represent a kind of diffraction pattern, have an interesting variation, reflecting the nontrivial dependence of the scattering amplitude on θ in (6.6).

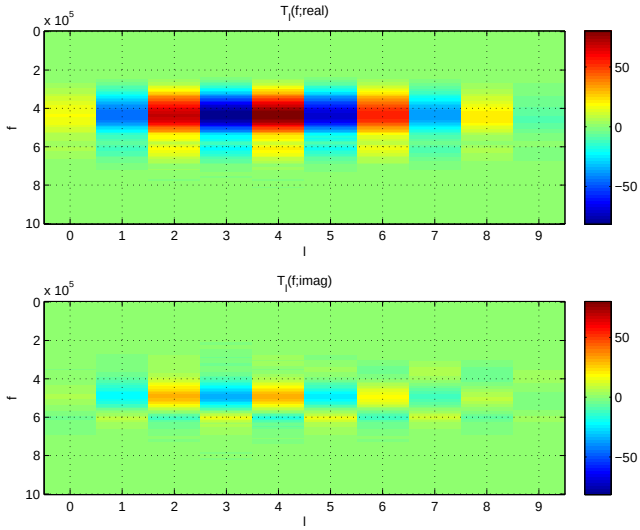

FIG. 17: Real and imaginary parts of the coefficients $T_l(k)$, $l = 0, 1, 2, \ldots, 9$ obtained from the scale tank data data (whose magnitude is shown in the lower panel of Fig. 16).

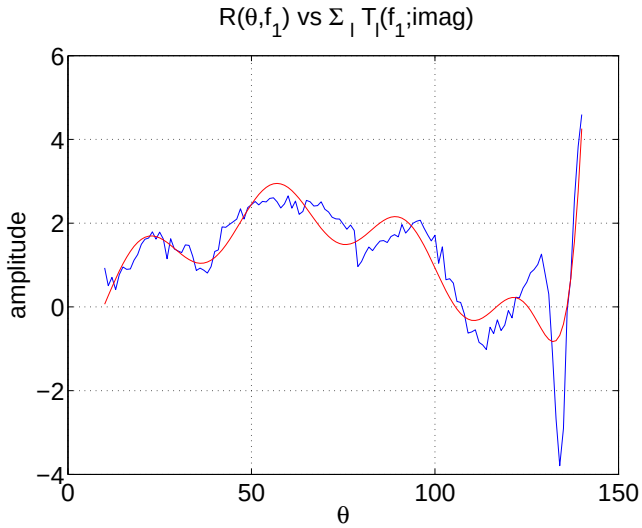

FIG. 18: Comparisons of the measured and reconstructed [using the 10 term series (7.1)] real part of the scattering amplitude $f(\theta, \omega)$ at the single frequency $f = 500$ kHz. A better fit would require a much larger value of $l_{\max}$, illustrating the increasing complexity of the diffraction pattern at higher frequency, especially as one approaches forward angle scattering where shadowing effects become strong. The fit has been performed over the limited range of angles $10° \leq \theta \leq 140°$ seen in the data in Fig. 16, where the direct blast interferes at the higher end and transmitter-receiver occlusion interferes at the lower end.

mitters to the 4 m BOSS. These could provide the added benefit of independently covering different frequency bands, leading to stronger ensonification of the environment and hence stronger scattering returns.

(b) *Multiple BOSS platforms, or at least a separate, independently controlled transmitter:* Obviously, multiple independently controlled platforms would lead to a huge gain in angular aperture. Of course this entails enormous technical difficulties as well, e.g., simultaneous control and simultaneous geolocation issues.

APPENDIX A: BOSS DATA ANALYSIS IN SUPPORT OF SEDIMENT INVERSIONS

This effort will consider the feasibility of determining sediment acoustic properties via remote acoustic measurements. While previous efforts [3, 4] have reported estimates of sediment properties via acoustic interrogation, this paper focuses on efforts to establish this sensing capability with in-situ data provided by the BOSS sonar system.

Figure 20 depicts the acoustic path lengths for the BOSS system configuration (Fig. 21). An omnidirectional source located 0.72 m aft of the receive array axis ensonifies the bottom and (assuming smooth surface, ray tracing theory) the geometric path that obeys the reflection law ($\theta_{incident} = \theta_{reflected}$) determines the respective path and delay for a particular source/receiver pair.

Given a dataset of forward-scattered returns, as seen across an array, we observe a sweep of incident angles as shown in Fig. 20. When the incident angle passes the critical angle, defined by $\sin(\theta_c) = c_1/c_2$ (see Sec. II A) the magnitude of the reflection coefficient will be unity and the phase changes in a distinctive way. This dependence on incident angle is shown in Fig. 1. Reflections past critical will have a distinct phase component that may be exploited to more accurately determine θ_c and hence c_2 from element-wise observations, where only amplitude variations are observable.

For the present geometry, we have calculated the available range of incident angle as shown in Fig. 22 for the cases of:

1. Blue: source is in the same longitudinal position as the arrays.

2. Red: source displaced 0.72 m backward.

The blue trace was a baseline check that shows the minimum critical angle, while the red trace shows the effect of longitudinal offset. For the array length of ~ 1.5 m and height off the bottom of 1.5 m we can achieve a range of $9° \leq \theta_{\text{incident}} \leq 25°$. Note that we are achieving this observable range of θ_{incident} by looking at the data across all the elements of the array. Unfortunately, for the anticipated sediment sound speed this range of θ_{incident} will only occupy the sub-critical angle regime of Fig. 1. Nonetheless, with a data set of adequate quality, we anticipate that an estimate of the reflection coefficient

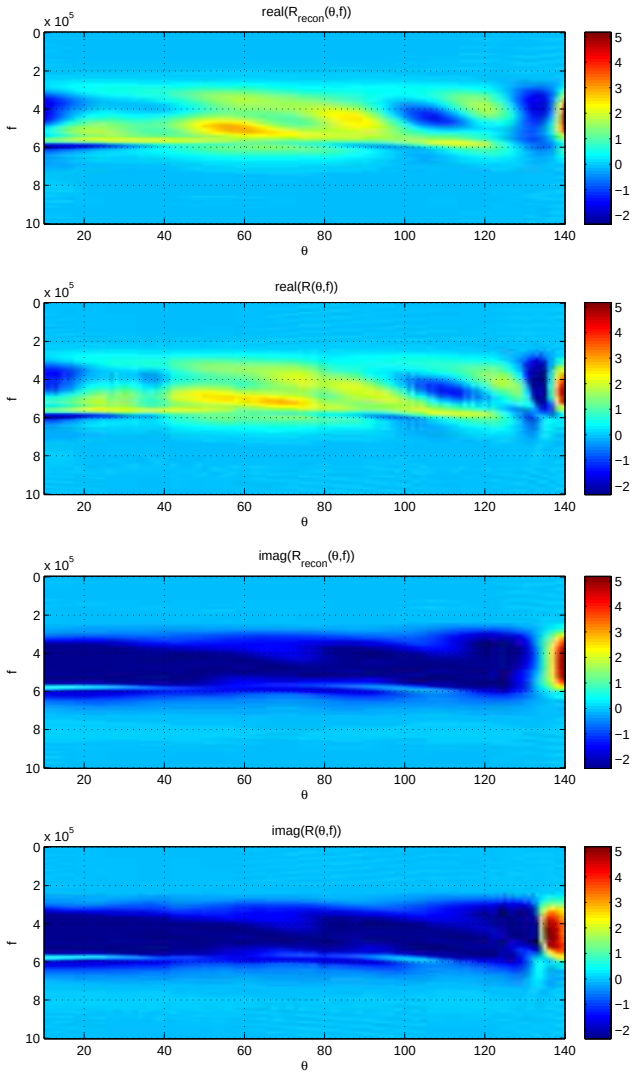

FIG. 19: Comparisons of the measured and reconstructed [using the 10 term series (7.1)] scattering amplitude $f(\theta, \omega)$ over all frequencies. The top two panels compare the real parts, the bottom two the imaginary parts. The fits are again seen to yield poorer results at higher frequencies at larger forward angles.

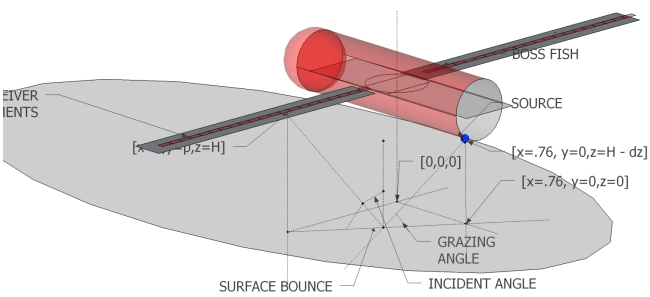

FIG. 20: Acoustic Path Lengths for BOSS Measurement

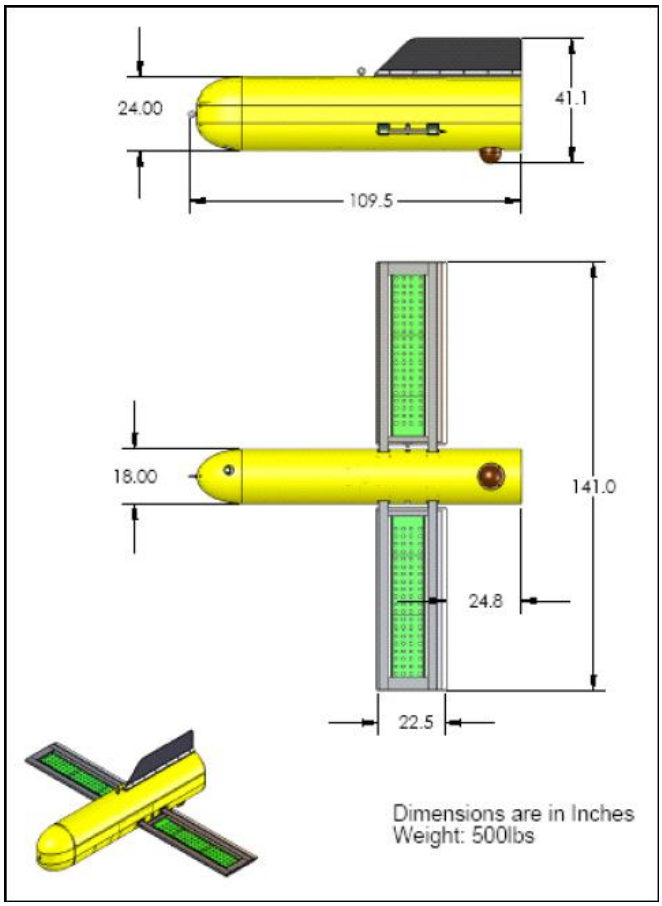

FIG. 21: Florida Atlantic University's 160 Channel BOSS towfish

can be developed by a ratio of direct to surface bounce returns at incident angles below critical.

1. Data Analysis

NSWC PCD staff are identifying the most suitable datasets for testing the proposed methodology for estimating reflection coefficients. All of the data that has been processed so far was collected by Florida Atlantic University using their 160 Channel BOSS towed system under SERDP project 1507, and is currently archived at NSWC PCD. The 160 Channel BOSS has a different system configuration that the 40 Channel BOSS system owned by NSWC PCD, and these differences have produced peripheral challenges over and above dataset selection. In order to develop an estimate of the reflection coefficient from a selected data set these issues must be considered:

1. Altitude H above seafloor.
2. Particulars of the seafloor parameters for the experiment.
3. Geometry of the array

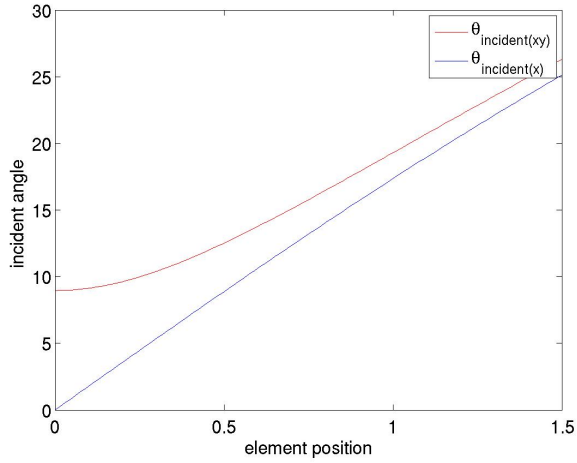

FIG. 22: Incident angle vs. array offset

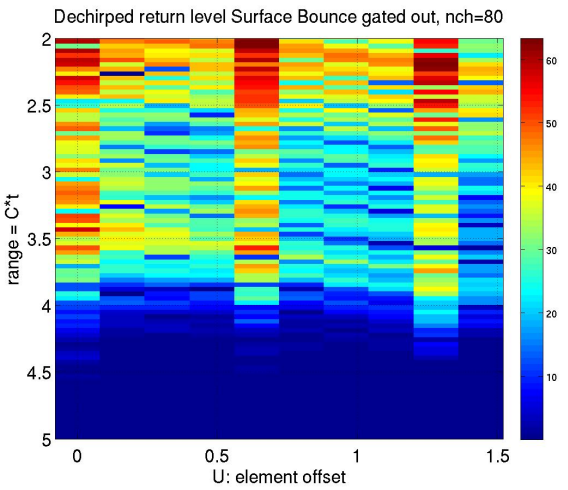

FIG. 23: Return level with channel gain variability

4. quality of retrieval "reader" software

Our recent experience has shown that retrieval of past datasets is particularly vulnerable to the quality of experimental documentation as it relates to system configuration parameters such as waveforms and source levels along with system design parameters such as the wiring of sensors for both channel allocation and consistent gain settings. This last point has a strong bearing on our reported results because the programming of the field-programmable gate array (FPGA) logic chip that interfaces the analog-to-digital converters (ADCs) to the hard drive storage has imposed two distinct and difficult unknowns into the data:

1. The channel indices are unknown (or at least undocumented) and require an iterative sequence of requesting data files from the "reader" format interface software (no source code available) and checking the candidate ordering against timing and beamforming metrics.

2. Channel gains are also indeterminate. For the most recent data set that has been provided "MediumSand$_{10chan}$" (medium sand sediment, and 10 nominally sequential channels extracted) it has been observed that every fourth element (Fig. 23) has an additional $\sim$ 18 dB of received level over and above its neighboring elements. This could be due to a glitch or feature or could be an inadvertent interchange of a low and high gain staves. Note that the reflection coefficient will vary approximately 3 dB across the range of sub-critical angles (Fig. 1). These issues only apply to the 160 Channel BOSS and it should be possible to do data collections specifically aimed at estimation of reflection coefficients with the 40 Channel UUV system that resides at NSWC PCD where there are no unknown parameters.

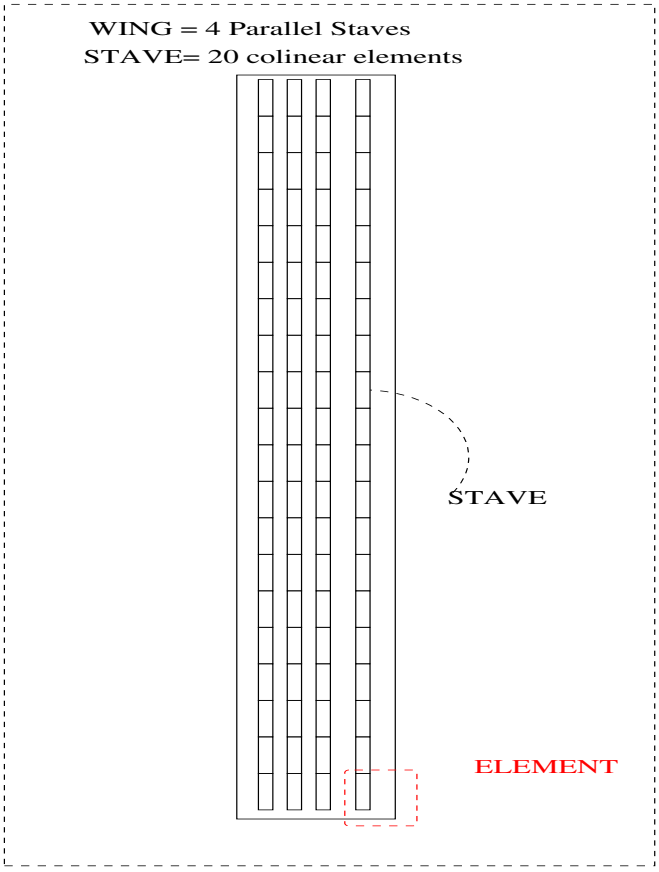

FIG. 24: BOSS array details

a. Hardware geometry and characteristics

Figure 24 shows the general layout of either the port or starboard sonar array for the BOSS fish of figure 21; Each wing has 4 parallel staves, and each stave consists

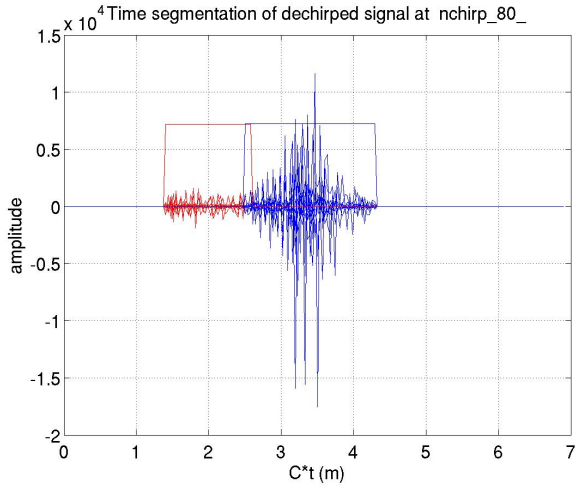

FIG. 25: Time segmentation for direct and bounce paths (nchirp=80)

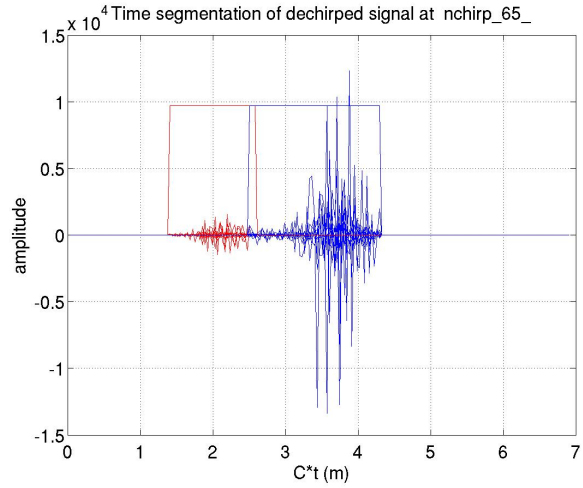

FIG. 26: Time segmentation for direct and bounce paths (nchirp = 65)

of 20 piezo-ceramic receive elements. The source element shown in Fig. 20 is an ITC1007. We are still trying to identify the electroacoustic specifics for the piezo receive elements. Another point is that given the nominal geometry of the experiment and the array there will be four distinct sensor returns at very nearly the same echo time. This particular geometry increases the difficulty in untangling the unknown channel indices.

b. *Inferring geometry from time segmentation and interpretation*

In order to observe the widest span of $\theta_{incident}$ the dataset "MediumSand$_{10chan}$" was chosen due to its low flying altitude of about 1.5 m from the bottom surface. The path length for the assumed geometry can be shown equal to

$$PL(x; SRC, RCV) = \sqrt{\Delta_y^2 + x^2} \tag{A1}$$

where x is the array element offset from the longitudinal CL and Δ_y is the longitudinal offset from the array/wing CL.

For the bottom bounce path the equivalent result is

$$PL(x; bounce) = 2\sqrt{H^2 + \left(\frac{PL(x; SRC, RCV)}{2}\right)^2} \tag{A2}$$

Figures 25 and 26 plot an overlay of slightly varying returns against $Range = Ct$ [11]. We plot against $R = Ct$ because the path lengths within the experiment include both one way (direct) and two way (bottom bounce) acoustic paths.

As seen in both figures the first bottom bounce resides at 3.2 m (1.6 m one-way) and there is a weaker return centered at ~ 2 m. These same returns are alternatively

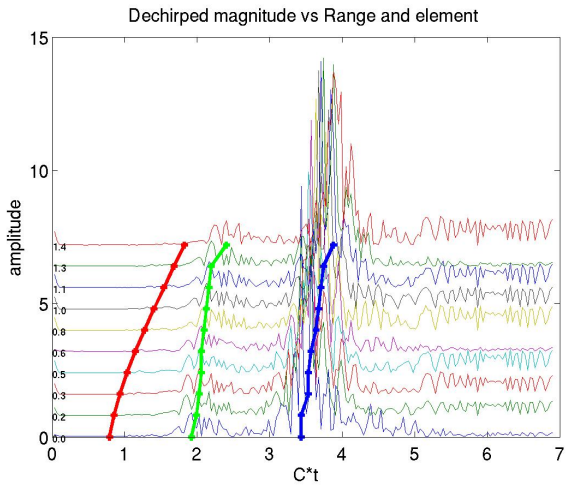

FIG. 27: Time/Element waterfall plot for dechirped returns (nchirp = 65)

plotted in pseudo-3D "waterfall" mode in Figs. 27 and 28 [12].

This waterfall mode provides distinct observations of each trace with the potential for more effective visual dynamic range. Hence, we can overlay the green- and blue-peak location traces that align with the early and later returns and along with a geometric prediction based on (A1) (red trace).

The difference between the respective figure pairs of [25, 26] and [27, 28] is the time extent of the dechirping waveform. We initially perturbed the notional pulse length because we were dissatisfied with the post dechirping range resolution of Fig. 28 and we found that reducing the time extent resulted in the sharper post dechirp resolution of Fig. 27. In the absence of a formal dechirp waveform specification (that would also reflect the free-field transceiver impulse response) we have used an ad-

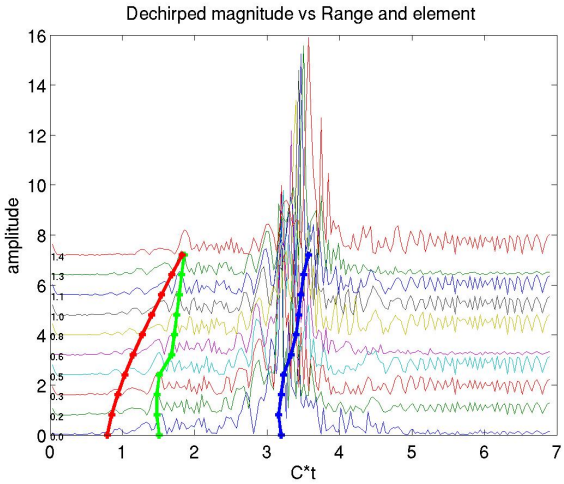

FIG. 28: Time/Element waterfall plot for dechirped returns (nchirp = 80)

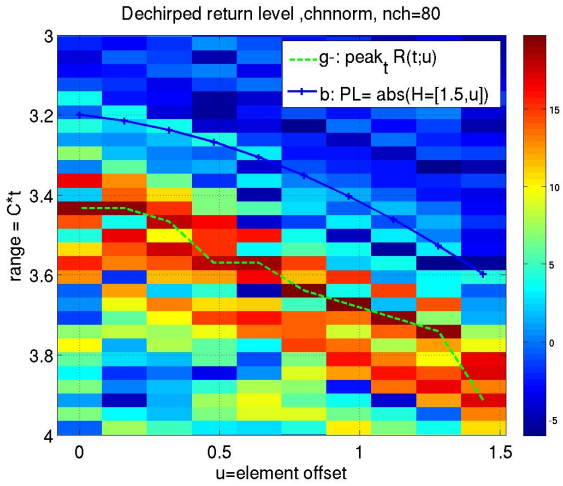

FIG. 29: Normalized return level vs. range and element

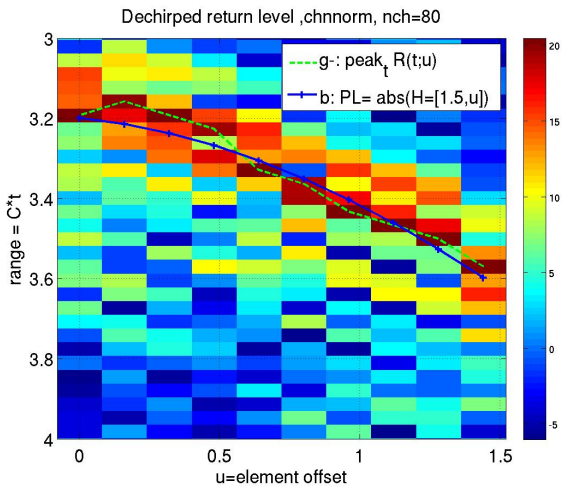

FIG. 30: Normalized return level vs. range and element

hoc procedure of iteratively autofocusing towards the sharpest dechirp signal. An alternate approach would involve identifying another dataset where increased height off bottom would provide a distinct time gap in the returns between the direct- and bottom-bounce returns. This would help untangle the ambiguity of the early and late arrivals and provide a direct experimental measurement for the transceiver impulse response. Other important observations that pertain to these figures include

1. The geometric prediction (red trace) is constant across Figs. 27, 28 but the early return peak location (green trace) varies with the FM dechirp specification: Post-dechirp time delay is affected by the signal model used in the dechirp.

2. The signal level difference for these first returns relative to the bottom bounce is roughly what would be expected by the geometric factor $G(f, \theta)$ discussed in App. B. However, the direct path $PL(x; SRC, RCV)$ characteristic (red trace) differs significantly from the green trace in Figs. 27, 28 The green trace does not agree with any viable hypothesis; 2 m is too far away for the one-way SOURCE/RECEIVER path and it is too close to explain as a round trip from a 1 m distance target.

Figures 29 and 30 show these same time and channel return in a dB color scale image that emphasizes return level over the time difference readily seen in the "waterfall" figures. (In fact, the return range was limited to exclude the first return and improve the dynamic range.) These plots highlight the close time arrival agreement for the bottom-bounce model when the altitude and dechirp-group delay are properly accounted for.

2. Conclusions and Recommendations

Our familiarity with the 160-channel BOSS data sets collected under SERDP project 1507 is improving, but still evolving. Presently there are four major impediments that must be addressed before we can step through a self-calibration (Sec. B) and curve-fitting procedure to estimate the reflection coefficient of the sediment:

1. Channel index indeterminacy: Knowing which data channel data we are looking at.

2. Gain indeterminacy: Know the gain factor for each channel.

3. Waveform indeterminacy: A more accurate signal model for the transceiver impulse response will improve the time resolution and reduce the bias of the amplitude estimation for the signal processing sequence.

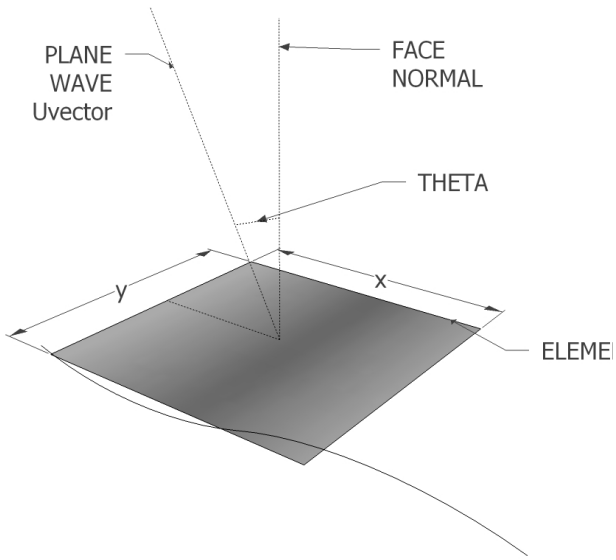

FIG. 31: Plane wave at angle to boresite

4. Geometric uncertainty: This involves reconciling timing and channel index to achieve better agreement with the geometric configuration.

We very much appreciate the time and effort that Rudy Arrieta has invested in providing us the initial datasets on such short notice. We anticipate that the above issues can be shortly resolved to achieve an in-situ R_{coeff} estimation capability. This remote sensing capability can then be used to support both of a T-matrix based inversion for detecting buried UXO objects.

APPENDIX B: SELF CALIBRATION

In some experimental setups (Fig. 20) adequate estimates of acoustic source level may not always be available. In this case, it may still be possible to estimate the reflection coefficient by determining the (amplitude) ratio of the bounce to the direct path.

Figure 31 shows a plane wave incident on a piezo element at an angle to the element's normal vector. The same linear model that develops the traditional beam pattern response for these elements can be extended all the way to $\pi/2$ from boresite which represents a plane wave traveling "along" the element's face (alternately $k_z = 0$).

This response,

$$G(f,\theta) = \int_{y_o}^{y_f} \int_{x_o}^{x_f} e^{i(k_x x + k_y y)} dx dy, \qquad \text{(B1)}$$

where $[k_x, k_y] = \frac{2\pi f}{C}[\sin(\theta), \cos(\theta)]$, is shown in Fig. 32 for parameters within the range of experimental data we are considering. As a result of the relatively small size of the element as compared to the λ the in-plane response

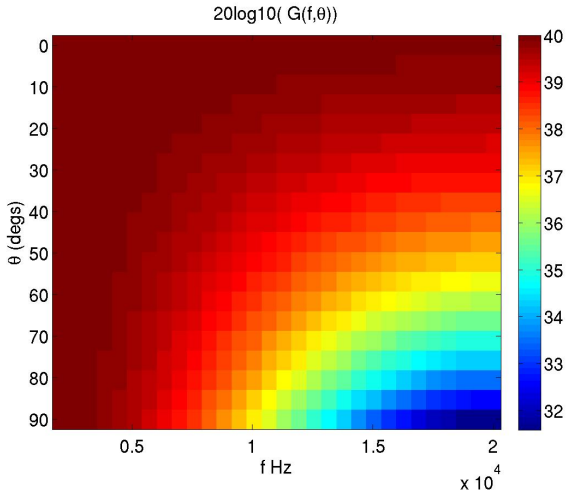

FIG. 32: Plane Wave response vs $G(f,\theta)$

is no more than 10 dB down from the boresite response. Moreover, for the configurations under consideration the geometric factor $kL \sim O(1)$ (L being the array's nominal dimension) is small enough to substantially avoid the side lobe issue. Hence, assuming $G(f,\theta)$ to be a consistent and distinct geometric factor for respective in-plane (direct) and near-boresite (bounce path) contributions, provides the potential to determine the ratio.

[1] These follow from continuity of $\hat{\varphi}$ and of $(1/\rho)\hat{\partial}_z\varphi$ across the boundary. They are identical to the TE polarized reflection and transmission coefficients for electromagnetic waves, with index of refraction $n_i = 1/c_i$ and permeability $\mu_i = \rho_i$. See, e.g., J. D. Jackson *Classical Electrodynamics* (John Wiley and sons, New York, 1975).

[2] A. Maguer, E. Bovio, W. L. J. Fox and H. Schmidt, "In situ estimation of sediment sound speed and critical angle," J. Acoust. Soc. Am. **108**, 987–996 (2000). Note that due to its porous nature, sediment acoustic propagation is dispersive at higher frequencies, and the phase speed $c_2(\omega)$ becomes frequency dependent.

[3] "Direct measurement of sediment sound speed in Shallow Water '06," J. Yang, D. Tang, and K. L. Williams, J. Acoust. Soc. Am. **124**, No. 3, Pt. 2 (2008).

[4] K. L. Williams, "Forward Scattering From a Rippled Sand/Water Interface: Modeling, Measurements, and Determination of the Plane Wave, Flat Surface Reflection Coefficient," IEEE Oceanic Eng. **34** 399–406 (2009)

[5] The entire analysis, of course, ignores such complicating features as absorption and bottom roughness, whose modeling would be required for more complex sediments.

See, e.g., D. D. Sternlicht and C. P. de Moustierc, "Time-dependent seafloor acoustic backscatter (10-100 kHz)," J. Acoust. Soc. Am. **114**, 2709–2725 (2003).

[6] The choice of this point is somewhat arbitrary, but it should lie on any symmetry axis of the target in order that the T-matrix embody this same symmetry. Similarly, locating it near the centroid of the target should lead to better decay properties of the coefficients for large index.

[7] R. Lim, J. L. Lopes, R. H. Hackman, and D. G. Todoroff, "Scattering by objects buried in underwater sediments: Theory and experiment," J. Acoust. Soc. Am. **93**, 1762-1783 (1993).

[8] I. S. Gradshteyn and I. M. Ryzhik, *Table of Integrals, Series, and Products* (Academic Press, 1980).

[9] E. Merzbacher, *Quantum Mechanics, 2nd Edition* (John Wiley & Sons, New York, 1970).

[10] It has recently come to our attention that there may be an upcoming proposal to SERDP to enhance BOSS in precisely this way (James Solinsky of EdgeTech, personal communication). We see this as a very exciting avenue of possible future collaboration.

[11] These returns have already been correlated (dechirped) against the transmit waveform.

[12] These plots have also had the respective channel gains adjusted such that each trace has the same RMS.